| Title | マルチグレイン構造を有するモデルZiegler-Natta触媒を利用した構造性能相関の解明 |
|---|---|
| Author(s) | 池田, 智博 |
| Citation | |
| Issue Date | 2022-03 |
| Type | Thesis or Dissertation |
| Text version | ETD |
| URL | http://hdl.handle.net/10119/17775 |
| Rights | |
| Description | Supervisor:谷池　俊明, 先端科学技術研究科, 博士 |

Doctoral Dissertation


# Fabrication of model multi-grain structures in Ziegler-Natta catalyst for investigation of structure-performance relationship


Tomohiro Ikeda


Supervisor: Professor Dr. Toshiaki Taniike


Japan Advanced Institute of Science and Technology

[Materials Science]

March 2022

# Preface

This dissertation is the result of the studies supervised by Professor Dr. Toshiaki Taniike during 2018-2022. The purpose of this dissertation is fabrication of model multi-grain structures in Ziegler-Natta catalyst for investigation of structure-performance relationship. Chapter 1 is a general introduction relative to the object of this study. Chapter 2 shows the bottom-up synthesis of model Ziegler-Natta catalyst using a spray dryer. Chapter 3 shows the synthesis of microfine grade UHMWPE using the secondary-particle model Ziegler-Natta catalyst. Chapter 4 shows MgO-based model Ziegler-Natta catalyst combined with donors for polypropylene synthesis. Chapter 5 is the summary of the conclusive items of this dissertation.

Tomohiro Ikeda

Taniike Laboratory

School of Materials Science,

Japan Advanced Institute of Science and Technology

# Contents

**Chapter 3**     **Bottom-Up Synthesized Ziegler-Natta Catalyst for Ultra-High Molecular Weight Polyethylene**

Chapter 1

# *General Introduction*

## *1.1. Introduction*

Polyolefin is a general-purpose plastic represented by polyethylene (PE) and polypropylene (PP). PE and PP are the most widely and commonly produced polymers, accounting for 31.2% and 22.7% of the global polymer market, respectively [1,2]. The global market for polyolefins as a whole is worth about $300 billion, with more than 180 million tons produced annually [3]. Polyolefins are characterized by their low cost, light weight, high melting point, high chemical resistance, and high strength, as well as their composition of only hydrogen and carbon, which means that they do not contain toxic substances such as chlorine or aromatic rings. Therefore, it is easier to recycle and reuse than other materials, making it a material with low environmental impact [4]. Polyolefins have a wide range of applications, from daily necessities such as packaging and containers to high performance materials such as automotive materials, due to their excellent mechanical properties and high moldability, and because of these characteristics, steady growth is expected in the future.

The present polyolefin industry is made up of various technologies, for example, catalysts, manufacturing processes, molding processes, and additives. In the field of catalysis, the catalysts used include heterogeneous catalysts such as Ziegler-Natta catalyst with Ti as the active species, Phillips catalyst with Cr as the active species, and

metallocene catalyst, which is an organometallic complex containing two cyclopentadienyl anions, as homogeneous catalysts. The Ziegler-Natta catalyst is an important catalyst used not only in 99% of polypropylene production, but also in the production of high density polyethylene and linear low density polyethylene. Ziegler-Natta catalysts have excellent features, for example, high activity, high stereospecificity, wide molecular weight distribution, excellent polymer morphology, and low cost. However, as the polyolefin industry is expected to grow further, it is desirable to improve and develop Ziegler-Natta catalysts to further increase the productivity and control the primary structure of polyolefins. The Ziegler-Natta catalyst was developed nearly 70 years ago, and related technological developments and basic research have been vigorously carried out.

## 1.2. Ziegler-Natta Catalyst

Karl Ziegler was successfully polymerize ethylene at ambient temperature and pressure using a mixture of titanium tetrachloride ($TiCl_4$) and organoaluminum compounds as a catalyst for the first time, in 1953 [5]. In the next year, Giulio Natta successfully produced polypropylene with an isotactic content of 30~40% using a similar catalyst system, and further succeeded in synthesizing polypropylene with a high isotactic content of 80~90%

by using titanium trichloride (TiCl$_3$) instead of soluble TiCl$_4$. [6].

The activity initial Ziegler-Natta catalyst for ethylene polymerization showed only about 2~3 kg-PE g$^{-1}$-Ti. Later, TiCl$_4$ catalysts supported on SiO$_2$ or Al2O3 were developed like Phillips catalysts, but their performance was not good enough to be used for the industry. In 1963, Solvay succeeded in dramatically improving the activity of the TiCl$_4$ catalyst system by supporting TiCl$_4$ on Mg(OH)Cl using the surface hydroxyl groups. In 1968~1969, Montecatini and Mitsui Petrochemical independently developed MgCl$_2$-supported TiCl$_4$ catalysts. This catalyst system is still used as the main catalyst for polyethylene production.

The catalysts for propylene polymerization require to control the stereospecificity in addition to high polymerization activity. The first generation of crystalline TiCl$_3$-AlEt$_2$Cl Ziegler-Natta catalyst had remarkably low polymerization activity and produced about 10 % of atactic polypropylene as a byproduct. Therefore, the research for improving stereospecificity was conducted from 1950s. As a result, Solvay succeeded in obtaining δ-TiCl$_3$ with a large specific surface area (100-200 m2-g-1) by extracting AA-type β-TiCl$_3$, produced by reduction of TiCl$_3$ with AlR$_3$, with isoamyl ether and then reacting it with TiCl$_4$ in 1972. The catalyst system with the electron-donating compound was called the second-generation Ziegler-Natta catalyst, which improved the polymerization activity

by about five times compared to the first generation catalyst and reduced the byproduct

of atactic polypropylene to 3~4%.

Later, Montecatini and Mitsui Sekiyu developed the third generation Ziegler-Natta

catalyst, a $TiCl_4$ catalyst supported on $MgCl_2$ with an electron-donating compound such

as ethyl benzoate (EB) as the third component, between 1971 and 1974 [7]. This catalyst

is prepared by co-grinding $MgCl_2$ and $TiCl_4$-external donor (ED) complexes or by treating

the co-grind of $MgCl_2$ and ED with thermal $TiCl_4$ and then washing with organic solvents.

This catalyst system eliminates the needs of demineralization of produced polymer. In

1980-1981, the importance of specific combinations of donors used in the preparation of

heterogeneous Ziegler-Natta catalysts, which is called internal donor (ID), and EDs used

during polymerization was found. For example, the addtion of organic acid diesters into

$MgCl_2/TiCl_4$ catalyst system and the addition of alkoxysilane compounds during

polymerization were found to exhibit excellent stereospecificity. However, the catalyst

system required the removal of 6-10% of the total atactic polypropylene. Therefore,

catalyst development became focused on finding more efficient methods for catalyst

preparation and more effective donor combinations.

As a result of various subsequent attempts, a new combination of electron-donating

compounds was discovered in the early 1980s. Alkyl phthalates were used as ID for

catalyst preparation, and alkoxysilanes or silyl ethers were used as ED. This catalyst

system had a better balance of productivity and stereospecificity than the catalysts using

EB. This catalytic system was initially called an ultra-active third-generation catalyst, but

was later called fourth-generation Ziegler-Natta catalyst because it is based on the use of

a completely different electron-donating compound pair.

In the late 1980s, a new type of electron-donating compound, the 1,3-diether compound,

was discovered. Using this compound as ID, extremely high activity and stereospecificity

can be achieved without the need for any external Lewis base. This catalytic system is

called the fifth-generation catalyst. The growth of the activity and stereospecificity of the

propylene polymerization catalyst is shown in Figure 1.1.
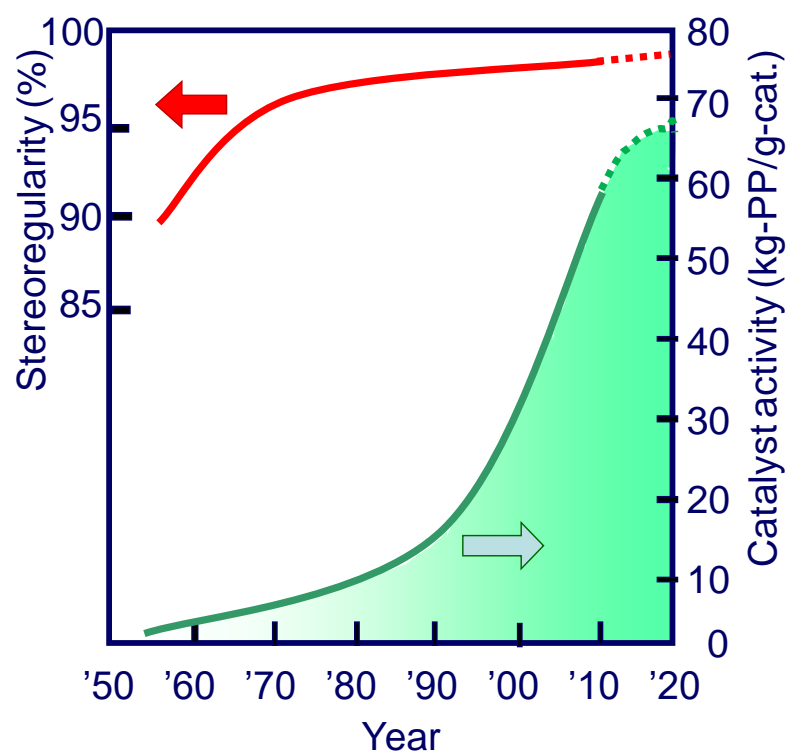
**Figure 1.1.** **The development of Ziegler-Natta catalyst for propylene**

**polymerization.**

## 1.3.   *Performance of Ziegler-Natta Catalysts*

### 1.3.1. Activity enhancement effect of MgCl$_2$

It has been reported that the remarkable activity enhancement effect of MgCl$_2$ is due to the increase in the active species concentration [C*] and the growth reaction rate constant kp. It is expected that [C*] increases in catalysts with highly dispersed Ti species, which can be active polymerization species, on MgCl$_2$ with relatively large surface area, but it is not easy to explain why kp increases. In order to confirm whether this effect is specific to MgCl$_2$ alone, Soga and co-workers used the Ti(OBu)$_4$/AlEt$_2$Cl/heptane system, in which the change in [C*] was considered to be small, and added 2-methyl-1-hexanol solutions dissolving various metal chlorides (M$_n$Cl$_n$) to the catalyst system, and compared the activity for propylene polymerization. As a result, a correlation between the polymerization activity and the electro negativity of M$_n^+$ ($\chi n = \chi 0(1+2n)$; $\chi 0$ = electro negativity of metal, n = oxidation number) was observed as shown in Figure 1.2.
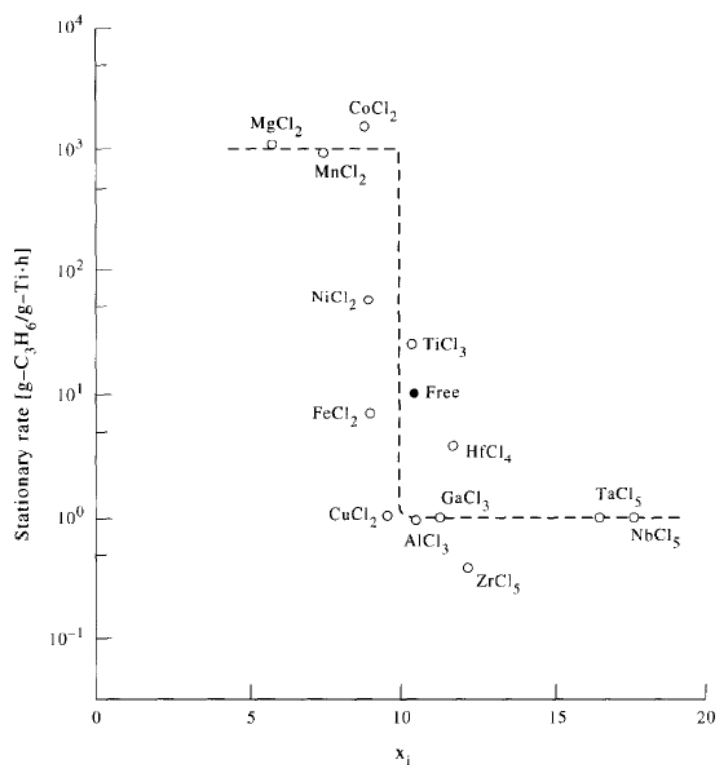
**Figure 1.2. Electroanegativity and steady state activity of metal ions.**

It was also found that the difference in activity was mainly due to the activation energy.

$M_nCl_n$ was added to typical Battele catalyst systems [$Cr(OAc)_3/AlEt_2Cl$, $Cr(OBu)_4/AlEt_2Cl$] and ethylene polymerization in toluene showed similar results. The same results were obtained when $MCl_n$ was added to [$AlEt_2Cl$, $Cr(OBu)_4/AlEt_2Cl$] and ethylene polymerization in toluene. These results can be interpreted as follows. First, coordination exchange occurs between $Cr(OAc)_3$, $Cr(OAc)_3$, or $Cr(OBu)_4$ and $AlEt_2Cl$, resulting in the formation of partially chlorinated metal compounds. These compounds then form a heteronuclear complex with $MCl_n$ via a chlorine bridge. When the electro-

9

negativity ($\chi_n$) of $M^{n+}$ is smaller than that of $Ti^{3+}$ ($Cr^{2+}$), electron donation from $M^{n+}$ to $Ti^{3+}$ ($Cr^{2+}$) occurs. As shown in Table 1-1, the binding energy of $Ti_{2p}$ increased with decreasing $\chi_n$ of the support. This is because the use of metal chlorides with small $\chi_n$, such as $MgCl_2$, $MnCl_2$, and $CoCl_2$, as a carrier, causes the reverse donation of electrons from the filled d-orbitals of $Ti^{3+}$ ($Cr^{2+}$) to the antibonding $\pi^*$orbitals of the coordinating olefin, which activates the coordinating olefin (weakening the C=C bond) and facilitates the insertion of $Ti^{3+}$ ($Cr^{2+}$). Escalona showed an accelerating effect on the polymerization rate when NaCl [$\chi$ ($Na^+$) = 2.7], $BaCl_2$ [$\chi$ ($Ba^{2+}$) = 4.5], $SrCl_2$ [$\chi$ ($Sr^{2+}$) = 5.0], $CaCl_2$ [$\chi$ ($Ca^{2+}$) = 5.0], $MgCl_2$ [$\chi$ ($Mg^{2+}$) = 6.0], and $BaCl_2$ [$\chi$ ($Ba^{2+}$) = 7.5] were used as $MCl_n$. This result is also in good agreement with the above reasoning. [8].

## 1.3.2. Mechanism of Lewis base

The mechanism of donors on the polymerization activity and the stereospecificity of the catalyst has not been fully elucidated because the internal and external donors can react with not only the active species (Ti) but also supports ($MgCl_2$) and co-catalysts ($AlR_3$).

Soga and co-workers investigated the correlation between Ti valence and olefin

polymerization activity. $Ti^{2+}$ was active only for ethylene, while $Ti^{3+}$ was active for several $\alpha$-olefins, including ethylene, propylene, 1-hexene, and 1,3-diene [9].

Busico et al. used $MgCl_2$/EB/$TiCl_4$-$AlEt_3$ catalyst system for the propylene polymerization in the absence of EDs and found that the polymer isotacticity (I.I.) decreased with increasing polymerization time. Busico et al. proposed that the cause of this phenomenon was the withdrawal of EB used as ID from the catalyst surface by $AlEt_3$, and the addition of EB as an ED was necessary to suppress the decrease of I.I. Besides, he proposed that there were three types of $Ti^{3+}$ as shown in Fig. 1-3 [10, 11]. Site-I and III are non-stereospecific sites, and Site-II is an isospecific site. Since the internal or external donor alone does not effectively enhance I.I., the ID selectively coordinates to the (110) surface of $MgCl_2$ and suppresses the formation of Site-III. On the other hand, the ED inhibits the elution of the internal donor and also selectively deactivates Site-I, which will improve I.I. However, this model could not explain the fact that the addition of EB increases the yield of isotactic polymer.
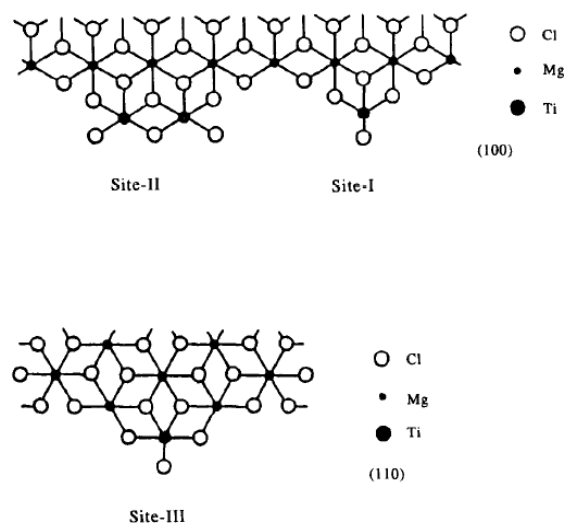
**Figure 1.3    Structure model of Ti³⁺ proposed by Busico et. al.**

Kakugo et al. used dichlorobenzene to column fractionate the isotactic portion of polypropylene obtained from several catalyst systems over a wide temperature range, and obtained results showing the weight, microtacticity, melting point, and isotacticity of each fraction. The maximum elution temperature of $\beta$-TiCl$_3$-AlEt$_2$Cl system was around 110°C, and that of $\delta$-TiCl$_3$-AlEt$_2$Cl system was around 120°C. The melting points and isotactic pentads of the eluted polymers increased linearly with increasing elution temperature, suggesting that the fractions were fractionated mainly by differences in the microstructure of the polymers. Therefore, $\delta$-TiCl$_3$-AlEt$_2$Cl would contain more isospecific active species than $\beta$-TiCl$_3$-AlEt$_2$Cl. They performed a similar study for the MgCl$_2$-supported TiCl$_4$ catalyst-AlEt$_3$ system, and the results are shown in Figure 1.5 and Figure 1.6 [12].

12

In the system without donors, the maximum elution temperature was around 110°C. However, when methyl p-toluate was added to this system, the maximum elution temperature shifted to around 120°C. I.I and isotactic pentad distribution of the fractions shown in Figure 1.4 and Figure 1.5, they concluded that isospecific active species are generated and proposed the active species model shown in Figure 1.6.
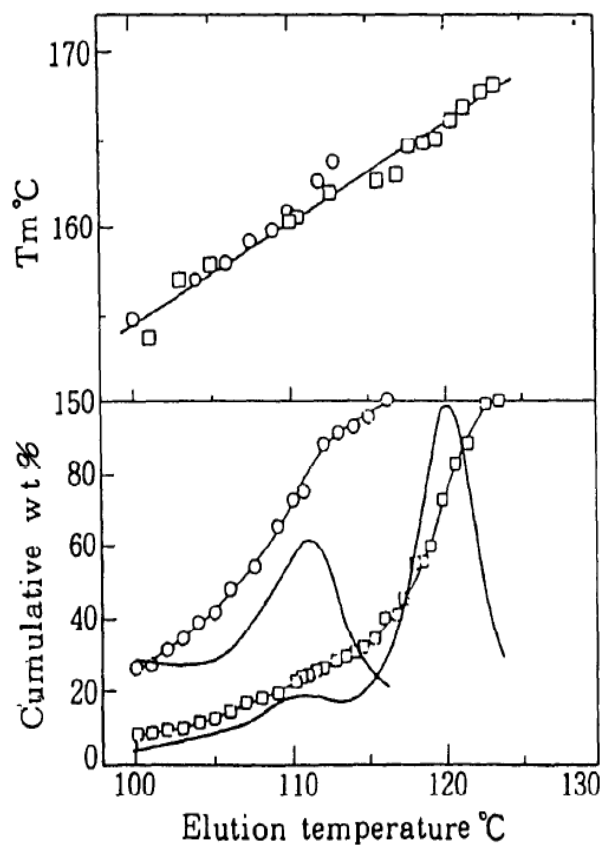


**Figure 1.4.   Cumulative and differential elution curves and melting point of the eluted polymer. (○) MgCl₂-supported Ti-AlEt₃ system, (□) MgCl₂-supported Ti-AlEt₃-*p*-toluic acid methyl ester system**
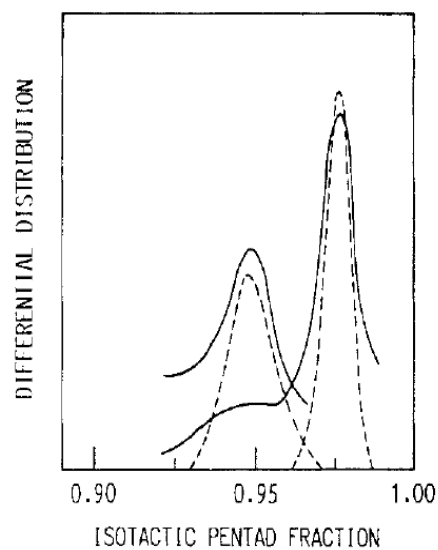
**Figure 1.5.** **Isotactic pentad distribution. (A) MgCl$_2$-supported Ti-AlEt$_3$ system, (B) MgCl$_2$-supported Ti-AlEt$_3$-$p$-toluic acid methyl ester system. Solid lines are experimental values and dotted lines are calculated values.**
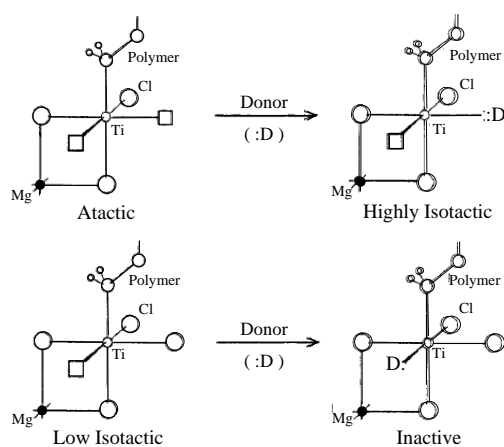


**Figure 1.6.** **Active species model for MgCl$_2$-supported Ti-based catalysts proposed by Kakugo et. al.**

Among the results shown by the various studies on donors, the generally supported effects of donor addition on the stereospecificity of catalysts are as follows [13].

14

- Inhibit the formation of non-stereospecific sites.

- Poisoning of non-stereospecific sites.

- Convert non-stereospecific sites to stereospecific sites.

- Convert stereospecific sites to highly stereospecific sites.

- To improve the reactivity of stereospecific sites.

### 1.3.3. Polymer morphology control

The morphology of the polymer obtained after polymerization is similar to the morphology of the catalyst used in any polymerization method. Since the development of the $MgCl_2$-supported Ziegler-Natta catalyst, the activity of the catalyst has been improved and, also, the ability to control the morphology of the polymer has been desired. In slurry polymerization, the use of a morphology-controlled catalyst with a stable shape makes it easier to handle the cleaning the wall of the reactor. Furthermore, good morphology catalysts can be used in high-productivity gas-phase polymerization and bulk polymerization.

Kakugo et al. observed the replication phenomenon by SEM of the stained polymer and found that the particles in the vesicles were one by one. The smaller particles in the

vesicles were observed in the polymer sample obtained by the higher activity catalysts. They proposed a model of polymer particle formation [14]. The image of the model is shown in Figure 1.7. The catalyst is fragmented by polymerization, and each of the particles forms a polymer vesicle and grows. As the polymerization progresses, the fragmentation of the particles inside the vesicles progresses, and smaller vesicles are formed in the bigger vesicles. A collection of these vesicles becomes the resulting polymer.
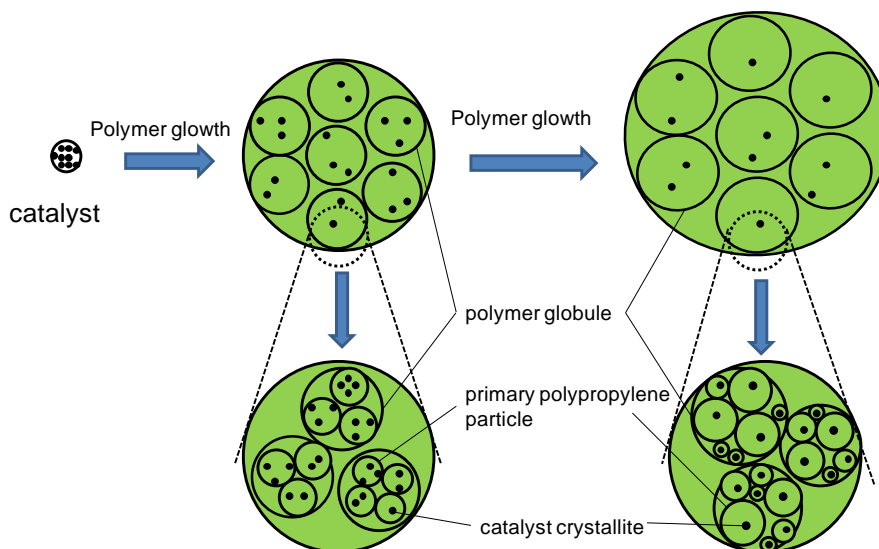


**Figure 1.7    The polymer particle formation mechanism proposed by Kakugo et al.**

## 1.3.4. Pore structure and fragmentation

Ziegler-Natta catalysts have a particle morphology called multigrain structure, which consists of an aggregation of nanometer-order primary catalyst particles. This porous

16

structure is thought to be closely related to catalytic performance through the diffusion of monomers and co-catalysts. However, the elucidation of the relationship between the structure and performance is very difficult because the catalyst structure continuously change during the polymerization due to the fragmentation. In order to investigate the effect of pore size on fragmentation, Weickert et al. succeeded in obtaining particles at the beginning of polymerization by shortening the polymerization time, and confirmed the difference in the degree of fragmentation process. The results are shown in Figure 1. 8 and Figure 1.9 [15]. In the case of the particles with small pores, only the outer part of the catalyst particle was fragmented and the polymer grew around it, whereas in the case of the particles with large pores, the entire particle was fragmented and the polymer grew in the gaps. This confirms that the pores affect fragmentation. This was the same as the result of a computer simulation of the same reaction [16].
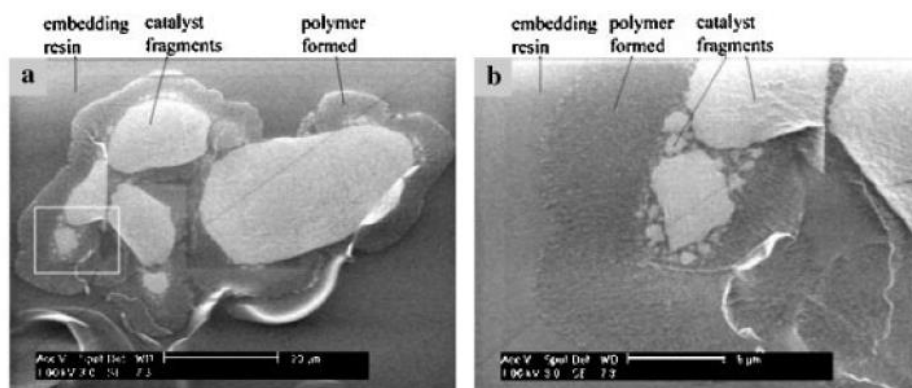
**Figure 1.8.    Cross-section of a particle in the initial stage of polymerization using**

**the catalyst with small pores.**
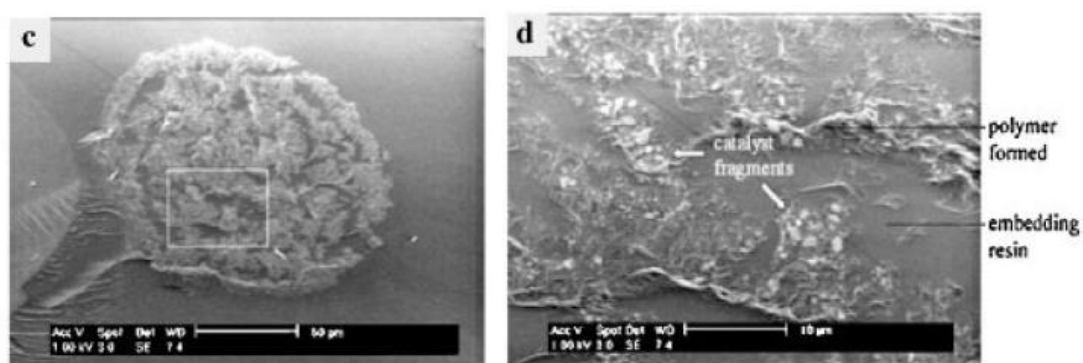


**Figure 1.9.    Cross-section of a particle in the initial stage of polymerization using**

**the catalyst with large pores.**

## 1.4. Objective of this study

In heterogeneous ZN catalysts, the catalyst particles consist of a hierarchical and irregular assembly of $MgCl_2$ particles, which are the primary structural unit, and have a variety of intraparticle pores from macro to micro size. Such a hierarchical structure is important for controlling the polymerization activity for a long time. This is because the fragmentation produced by polymerization destroys the carrier structure and continuously supplies new active sites that were buried in the pores. However, due to this complexity, it is very difficult to quantify the potential correlation between the support structure and the polymerization performance of a typical ZN catalyst. Even the simple relationship between catalyst surface area and activity is difficult to elucidate. Marigo et al. studied the correlation between propylene polymerization activity and catalyst surface area using several ZN catalysts prepared from $MgCl_2$-alcohol adducts [17]. There was no correlation between the activity and BET specific surface area, but there was some correlation with the surface area obtained by small angle X-ray scattering. Taniike et al. used the αS-plot method to investigate the validity of the BET surface areas of $MgCl_2$-alcohol adduct and $Mg(OEt)_2$-based ZN catalysts [18]. αS-plot revealed the presence of two classes of micropores, which prevented a physically meaningful evaluation of the BET surface area. In order to solve these problems, Taniike et al. adopted a model catalyst approach [19].

They developed a MgO/MgCl$_2$/TiCl$_4$ core-shell catalyst. A series of core-shell catalysts were prepared by treating single crystalline MgO nanoparticles with various dimensions and surface areas with TiCl$_4$. In these core-shell catalysts, the non-porous, unfragmented MgO core is thinly covered with the catalytic component. By using non-porous particles with an unfragmented MgO crystalline core, we were not only able to systematically vary the catalyst surface area by changing the particle size, but also to establish for the first time a clear proportional relationship between propylene polymerization activity and BET surface area [19, 20].
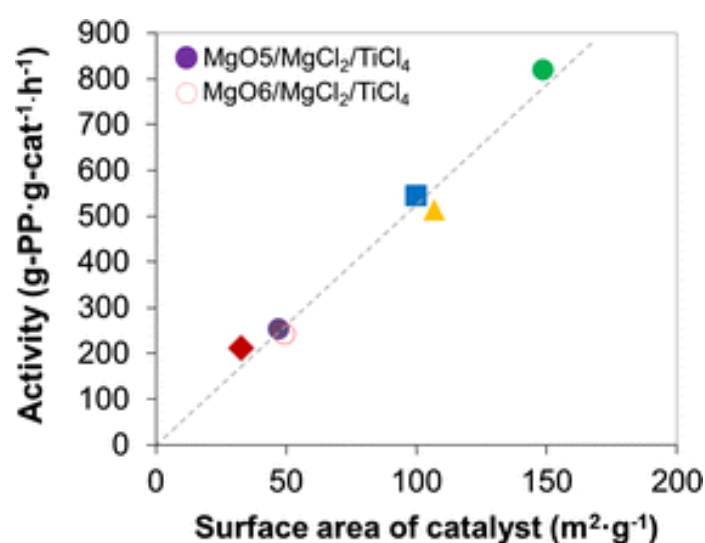


**Figure 1.10.    Relationship between the catalyst surface area and propylene**

**polymerization activity.**

In chapter 2, inspired by the fact that MgO/MgCl$_2$/TiCl$_4$ core-shell catalysts can maintain the morphology of raw MgO nanoparticles, secondary particle supports with a multi-grain structure were prepared by spray-drying MgO nanoparticles. The multi-grained catalyst was prepared by treating the secondary particle supports with TiCl$_4$. Homopolymerization of ethylene and propylene and copolymerization with 1-hexene were carried out with the primary and the secondly particle catalyst. The multi-grained catalyst had higher activity than the MgO/MgCl$_2$/TiCl$_4$ core-shell catalysts. On the other hand, both catalysts showed similar the kinetic profile in ethylene and propylene polymerization. The multi-grained catalyst possessed only macropoers and it wad found that macropore did not affect the diffusion limitation of the co-catalyst and the monomers.

In Chapter 3, ultra-high molecular weight polyethylene (UHMWPE) was produced using the multi-grained catalyst. MgO/MgCl$_2$/TiCl$_4$ core-shell catalysts can synthesize sub-micron grade (< 5 μm) UHMWPE, which started to melt at lower temperature in compression molding compared to the normal grade (> 70 μm) one. However, MgO/MgCl$_2$/TiCl$_4$ core-shell catalysts are not suitable for the synthesis of microfine grade (5~70 μm) UHMWPE due to their small particle size. A spray dryer was used to granulate MgO nanoparticles into tens of micrometer-sized secondary particles to prepare a catalyst support capable of synthesizing microfine grade UHMWPE. By increasing the

MgO slurry concentration fed to the spray dryer, the particle size of obtained support increased. The activity of the multi-grained catalyst had about 1.5~2 times higher activity compared to MgO/MgCl$_2$/TiCl$_4$ core-shell catalyst since the surfactant used to disperse the MgO/MgCl$_2$/TiCl$_4$ core-shell catalyst was not necessary for the multi-grained catalysts. The obtained polymer sample had the sphere shape and its size was about 50 μm. The synthesis of microfine grade UHMWPE was achieved by the multi-grained catalyst.

In Chapter 4, the multi-grained catalyst with a donor was prepared to improve the tacticity of the polypropylene. Ethylbenzoate and Cyclohexylmethyldimethoxysilane were used as an internal donor and an external donor, respectively. With the donors, the meso pentad of polypropylene increased.

# *Reference*

[1] Nowlin, T.E., New York: Wiley Scrivener Publishing, 2014, p. 403.

[2] Stalzer, M.M., Delferro, M., and Marks, T.J., *Polyolefins.Catal.Lett*., 2014, vol. 145, p. 3.

[3] Makaryan, I.A., and Sedov, I.V., Russian Journal of General Chemistry, 2020, Vol. 90, No. 6, pp. 1141–1162.

[4] 次世代ポリオレフィン総合研究会編, *次世代ポリオレフィン総合研究*, 2008, 3.

[5] K. Ziegler, H. Breil, H. Martin, E. Holzkamp, *German Patent* **1953**, 973, 626.

[6] G. Natta, P. Pino, P. Corradini, F. Danusso, E. Mantica, G. Mazzanti, G. Moraglio, *J. Am. Chem. Soc*. **1955**, *77*, 1708.

[7] Montedison, *Belgian Patent* **1972**, 785, 332.

[8] R. B. Seymount, T. Cheng Eds., K. Soga, *History of polyolefins*, 243

[9] K. Soga, T. Sano, R. Ohnishi, *Polym. bull*. **1979**, 4, 157

[10] V. Busico, P. Corradini, D. Martino, A. Proto, V. Savino, E. Albizzati, *Makromol. Chem.* **1986**, *187*, 1115.

[11] V. Busico, P. Corradini, A. Ferraro, A. Proto, V. Savino, E. Albizzati, *Makromol.Chem*. **1986**, *187*, 1125.

[12] M. Kakugo, T. Miyatake, Y. Naito, K. Mizunuma, *Macromolecules* **1988**, *21*, 314.

[13] Y. Arai, T. Fujita, *Japan Patent, 2010-30924, A,* **2010**.

[14] M. Kakugo, H. Sadatoshi, J. Sakai,*CATALYTIC OLEFIN POLYMERIZATION* **1989**, 563, 45-354

[15] B. Horackovaa, Z. Grofb, J. Kosek, *Chem. Eng. Sci*., *62*, **2007**, 5264-5270

[16] X. Zheng, M. S. Pimplapure, G. Weickert, J. Loos, *Macromol. Rapid Commun., 27*, **2006**, 15-20

[17] Marigo A, Marega C, Zannetti R, Morini G, Ferrara G (1921) Eur Polym J 2000:36

[18] Taniike T, Chammingkwan P, Thang VQ, Funako T, Terano M (2012) Appl Catal A 24:437

[19] Taniike T, Chammingkwan P, Terano M (2012) Catal Commun 27:13

[20] Chammingkwan P, Thang VQ, Terano M, Taniike T, Top. Catl. (2014) 57, 911-917.

Chapter 2

# *Bottom-Up Synthesis of Multi-Grained Ziegler–Natta Catalyst Based on MgO/MgCl₂/TiCl₄ Core–Shell Catalyst*

## *2.1. Introduction*

Morphology influences the performance of solid catalysts through the diffusion of reactants and heat. Particle morphology influences the performance of solid catalysts, as it dictates the mass transport and heat transfer phenomena during catalysis. This is often found in catalyzed gas-phase polymer production, where the gaseous monomer is converted to a solid polymer by the active sites distributed throughout a catalyst macroparticle. Thus, it is essential to obtain spherical catalyst macroparticles with sufficient strength to prevent the formation of fine particles during the reaction [1]. In fact, such a stringent requirement of particle morphology is unique to solid catalysts employed for polymer production at the industrial scale.

Heterogeneous Ziegler–Natta catalysts (ZNCs) are widely used in the synthesis of polyolefins (polyethylene (PE), polypropylene (PP), and relevant copolymers, etc.). In ZNCs, Ti species (mostly $TiCl_4$) adsorbed on $MgCl_2$ support form active species by contacting with an alkylaluminum reagent. The catalyst before being activated is called a pre-catalyst. The mainstream preparation method is based on a top-down approach of the chlorination of spherical Mg precursors (representatively, $MgCl_2$ alcohol adduct and $Mg(OEt)_2$), which results in effective pre-catalysts, from the viewpoint of performance and morphology control. Regardless of the types of raw materials, such a top-down

method produces a pre-catalyst with spherical macroparticles of micro-meter size and qualitatively similar interior structures. There are various sizes of pores within a macroparticle, originating from the hierarchical aggregation of primary catalyst particles. These primary particles are made of $TiCl_4$ adsorbed on lateral surfaces of $MgCl_2$ nanocrystals with a lateral dimension of about 5–10 nm and a thickness of 1–2 nm [2]. This interior structure of a macroparticle, on the basis of the aggregation of primary particles, is referred to as the multi-grain structure. The multi-grain structure and its function have been studied both experimentally and theoretically [3–5]. It has been revealed that the size and distribution of pores affect the diffusion of reagents, and thus the proportion of polymers grown on the outer surface of the catalyst particles and inner surfaces of the pores formed in the early stages of polymerization. In the subsequent stages of polymerization, the growing polymer inside the pores induces the fragmentation of the catalyst macroparticle by the hydraulic power, exposing fresh Ti species. Continuation of the polymer growth and the fragmentation processes cause the synthesized polymer particles to mimic the morphology of the catalyst macroparticle (so-called replica effect) [6–8]. Therefore, the multi-grain structure of catalyst particles nicely explains the fact that immediately after the start of the polymerization reaction, the catalyst activity is small, but gradually increases as polymerization proceeds, and, finally,

remains high for a relatively long period of time (build-up-type kinetics). Such polymerization kinetics is feasible as the multi-grain structure helps to avoid undesirable phenomena, such as atomization, due to crushing of the catalyst/polymer particles by rapid reaction and deactivation, due to localized heating. On the other hand, a method to control the multi-grain structure has not been established yet. Even though a few model catalysts with primary particles made of fused silica or polystyrene were employed to investigate the role of the particle interior structure in diffusion and polymer particle growth, such catalysts hardly represent the industrially applied ZNCs. Therefore, to study the multi-grain structure of ZNCs, the bottom-up development of a catalyst with $TiCl_4/MgCl_2$ as the primary particle is interesting and important in its own right.

Previously, we have developed a $TiCl_4/MgCl_2/MgO$ core–shell catalyst by treating MgO nanoparticles with $TiCl_4$. In this catalyst, only the surface of the MgO particles was converted into a $MgCl_2/TiCl_4$ catalyst overlayer, while the center remained as MgO. Because the catalyst overlayer is very thin (1–2 nm), all the Ti species of the catalyst remain exposed from the beginning during the polymerization, and no new active sites are formed, due to fragmentation. In heterogeneous ZN catalysis, due to the transient nature of the catalyst during polymerization, it is difficult to relate the catalytic activity to even the surface area, which is a most basic structural characteristic. Using the

TiCl$_4$/MgCl$_2$/MgO core–shell catalyst, we demonstrated, for the first time, that the activity of a ZNC is proportional to the BET-specific surface area of its pre-catalyst [9]. The combined advantages of a relatively simple preparation protocol and low Cl content carried over to the final product inspired us to apply the core–shell catalyst to the production of ultra-high-molecular-weight polyethylene (UHMWPE) [10]. Furthermore, by treating the raw MgO nanoparticles with a surfactant (polyoxyethylene alkylamine, PA), the catalyst with a nanometer-sized diameter could be fully dispersed in heptane. The UHMWPE powder synthesized in this way had an extremely small particle size and a lesser degree of entanglement, thus being significantly advantageous for compression molding applications [11,12].

Here, we propose a bottom-up synthesis protocol of a multi-grain catalyst, on the basis of this core–shell catalyst. The spray-drying of MgO nanoparticles gives spherical secondary agglomerated macroparticles, and the subsequent TiCl$_4$ treating provides a secondary agglomerated catalyst with the core–shell catalyst as primary particles. In this method, the morphology of the primary catalyst particles and the secondary agglomerated macroparticles can be individually modified by the morphology of the raw MgO nanoparticles and the spray-drying conditions, respectively. Therefore, it has the potential to enable us to systematically study the relationship between the multi-grain structure and

29

its catalytic function, which has not been realized so far. In this paper, we report the basic preparation method of the bottom-up multi-grain catalyst, the results of its characterization, and performance evaluation in the homo-polymerization of ethylene, propylene, and their copolymerization with 1-hexene.

## 2.2. Experimental

### 2.2.1. Materials

MgO nanoparticles with a mean particle size of 50 nm (MgO50), methanol, and

titanium tetrachloride (TiCl$_4$) were purchased from FUJIFILM Wako Pure Chemical Co.,

Ltd. and used as received. *n*-Heptane (Wako Pure Chemical Co., Ltd., Osaka, Japan) was

used after dehydration by bublling with molecular sieve 4A for 2 h. Ethylene of

polymerization grade (Sumitomo Seika Chemicals Co., Ltd., Osaka, Japan) and

propylene of polymerization grade (Japan Polypropylene Co., Tokyo, Japan) were used

as received. Further, 1-Hexene (purity > 97%, Sigma-Aldrich Co. LLC,St. Louis, MO,

USA) was used after dehydration by N$_2$ bubbling for 2 h in the presence of molecular

sieve 4A. Triisobutylaluminum (TIBA) donated by Tosoh Finechem Corp. was used after

dilution in heptane (1 mol L$^{-1}$).

### 2.2.2. Spray-Drying of MgO Nanoparticles

A schematic diagram of the spray-drying apparatus is shown in Figure 1 (Tokyo

Rikakikai, SD-1010). Pristine MgO nanoparticles (MgO50) were dispersed in water or

methanol by means of ultrasonication for 6 h to prepare a feeding slurry. The feeding

slurry was introduced into the atomizer by a peristaltic pump and sprayed into the main

chamber by compressed air. The sprayed droplets were dried by hot air in the main

chamber where extremely large dried particles fell into the separation container, and the

rest were carried over to the cyclone. Particles of a certain size were collected as a spray-

dried product (denoted as S-MgO50) by centrifugal force, and fine particles were flown

out to the exhaust line. The parameters for spray-drying are feeding slurry concentration,

feeding rate, inlet temperature, atomization air pressure, and blowing rate.
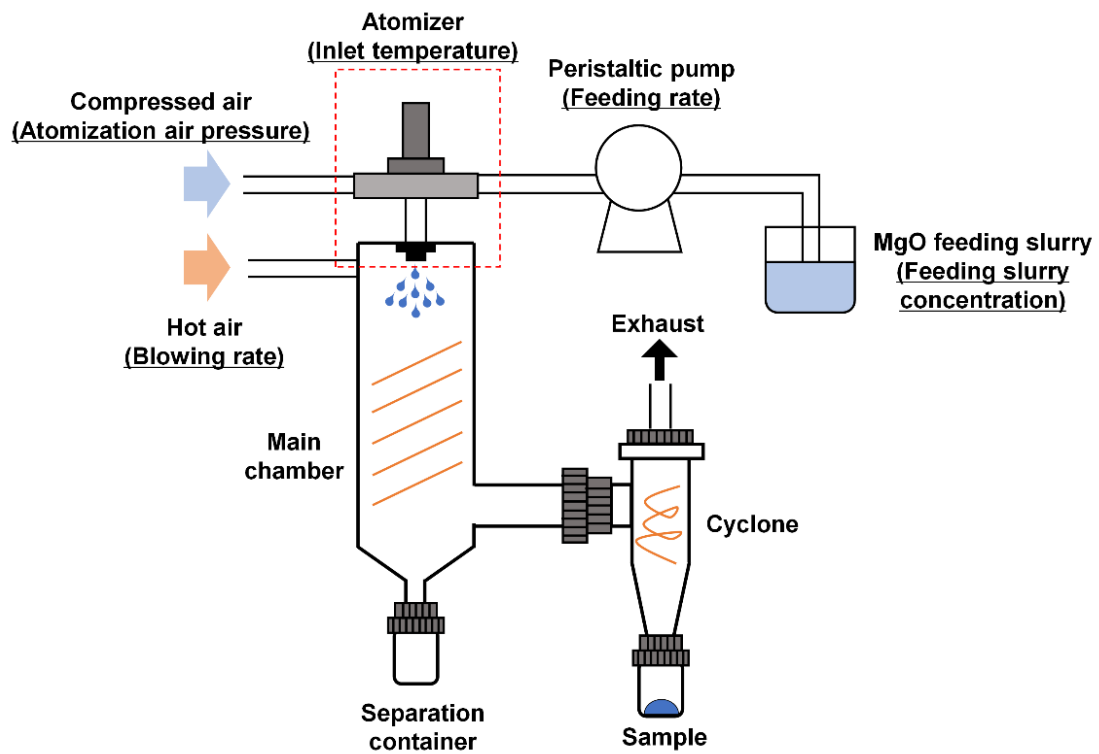


**Figure 1.    Schematic diagram of the spray-drying apparatus.**

### 2.2.3. Catalyst Synthesis

Then, 0.5 g of S-MgO was heated at 130 °C under $N_2$ flow for 6 h to remove physisorbed water before treating with 30 mL of $TiCl_4$ at the reflux temperature for 2 h. The obtained product (denoted as S-Cat50) was washed with heptane repetitively and stored as a slurry under $N_2$. For the sake of comparison, two reference samples (Cat50 and PA-Cat50) were prepared from non-spray-dried MgO50. For Cat50, the same procedure explained above was exploited except the fact that pristine MgO50 was used instead of S-MgO50. In the case of PA-Cat50, organic modification of MgO50 was performed using polyoxyethylene alkylamine (PA) to assist full dispersion of MgO nanoparticles in heptane prior to chlorination in heptane. The detailed procedure was reported in our previous paper [11].

### 2.2.4. Polymerization Test

Ethylene and propylene homo-polymerization were carried out in a 1 L stainless steel autoclave. After $N_2$ replacement in the autoclave, 300 mL of heptane as a solvent was introduced to the reactor and then saturated with 0.5 MPa of ethylene or propylene at 50 °C for 30 min. Following the addition of 2.0 mmol of TIBA as a co-catalyst, then, ca. 30 mg catalyst was introduced to initiate polymerization. The polymerization was carried

out at a constant pressure of 0.5 MPa for a predetermined time of 1 to 60 minutes at 50 °C. with stirring at 500 rpm.

Copolymerization of ethylene or propylene with 1-hexene was also performed using the same procedure, except a specified amount of 1-hexene was introduced just after the addition of heptane. The concentration of 1-hexene was set as 0.4, 0.8, 1.2 or 2.4 mol $L^{-1}$, and the total volume of heptane and 1-hexene was set to 300 mL. After 30 min of polymerization, the resultant polymer was filtered and dried at 60 °C in a vacuum oven for 6 h. The heptane-soluble polymer was collected by pouring the filtrate into 1 L of cold acetone. The precipitate was filtered out and dried using the same procedure.

### 2.2.5. Characterization

Morphologies of catalyst and polymer particles were observed using scanning electron microscopy (SEM, S-4100, Hitachi, Tokyo, Japan), which was performed at an accelerating voltage of 20 kV. The elemental distribution of catalyst components in polymer was analyzed on a cross-sectioned polymer particle using energy-dispersive X-ray emission (EDX, JCM-6000PLUS, JEOL Ltd., Tokyo, Japan) operated at an accelerating voltage of 15 kV. The polymer particle was cut by a razor chilled with liquid $N_2$. Before the SEM and EDX measurements, the sample was subjected to Pt sputtering

for 90 s.

Particle characteristics of a support and a catalyst were analyzed by light scattering (Partica LA-950V2, Horiba , Tokyo, Japan) in heptane. The particle size of samples is described with $D_{10}$, $D_{50}$, and $D_{90}$, which correspond to the particle size at 10, 50, and 90% of the cumulative volume-base particle size distribution. A relative span factor (RSF) was calculated based on Equation (1), as follows:

$$RSF = \frac{D_{90} - D_{10}}{D_{50}}, \tag{1}$$

XRD measurements were performed using MiniFlex600 (Rigaku Co.) with CuKα radiation at an acceleration voltage of 40 kV and a current of 30 mA in the $2\theta$ range of 3–90° with a scanning speed of 10°/min.

$N_2$ adsorption and desorption isotherms at 77 K were acquired on a BELSORP-max instrument (Microtrac BEL Corp., Osaka, Japan). Prior to the measurement, 20–50 mg of sample powder was outgassed at 80 °C over 2 h.

The Ti content was determined by UV–vis spectroscopy (V-770, JASCO, Tokyo, Japan). A measured amount of a catalyst was dissolved in $HCl/H_2SO_4$ solution, and then $H_2O_2$ was added to form a Ti–peroxo complex that exhibits the absorbance of the ligand metal charge transfer at 410 nm. The Ti content was analyzed from the intensity of the spectrum peak located at 410 nm using a pre-determined standard curve.

The copolymer samples were analyzed by NMR (Bruker 400 MHz) operated at 120 °C. About 40 mg of a copolymer sample was dissolved in 0.2 mL of 1,1,2,2-tetrachloroethane-$d$2 (internal lock and reference) and 0.5 mL of 1,2,4-trichlorobenzene containing 0.006 wt.% of 2,6-di-tert-butyl-4-methylphenol (stabilizer for heat degradation of polymer). The content of 1-hexene in the copolymer samples was determined with $^{13}$C NMR spectra (the number of scan = 5000). The chemical shift assignments were performed according to the works of Randall [21] and Kissin [22]. The stereoregularity of PP unit (*mmmm*) in the polymers was determined by the methyl peaks in the $^{13}$C NMR spectrum [23].

## 2.3. Results and Discussion

In order to realize catalyst macroparticles with the $MgO/MgCl_2/TiCl_4$ core–shell catalyst as primary particles, spray-drying of MgO nanoparticles (MgO50) was performed, using water as the dispersant. The summary of the screening of the spray-drying conditions is reported in Table S1. Feed rate, atomizing air pressure, feeding slurry concentration, and blowing rate of hot air to the main chamber were screened within the framework of conditions available for the instrument (Figure 1). No noticeable effect of spray-drying conditions on the MgO particle properties was observed, except that the particle morphology and size distribution deteriorated upon lowering the feeding slurry concentration. Thus, considering the results of Table 1, the recommended parameters by the manufacturer were chosen as a standard condition set. The spray-dried particle sample obtained with the standard condition set (S-MgO($H_2O$)) exhibited a narrow particle size distribution, with its peak top positioned at around 4 µm (Figure 2A), and the particles appeared in a spherical shape (Figure 2C). On the other hand, in the SEM image with a higher magnification (Figure 2C'), it was found that S-MgO($H_2O$) was an aggregate of particles with a plate-like texture that was clearly different in size and morphology from the raw MgO nanoparticles (Figure 2B).

**Table 1. Screening of spray-drying conditions for water dispersant.[1]**

| Condition | Feed rate (mL h$^{-1}$) | Atomization air pressure (kPa) | Slurry concentration (g L$^{-1}$) | Blowing rate (m$^2$ min$^{-1}$) | $D_{10}$ (µm) | $D_{50}$ (µm) | $D_{90}$ (µm) | RSF |
|---|---|---|---|---|---|---|---|---|
| 1 | 500 | 250 | 2 | 0.6 | 2.18 | 3.73 | 6.20 | 1.07 |
| 2 | 200 | 250 | 2 | 0.6 | 2.70 | 4.36 | 6.85 | 0.95 |
| 3 | 400 | 250 | 2 | 0.6 | 2.08 | 3.52 | 5.73 | 1.04 |
| 4 | 450 | 250 | 2 | 0.6 | 2.30 | 4.08 | 6.83 | 1.11 |
| 5 | 625 | 250 | 2 | 0.6 | 2.70 | 4.30 | 6.61 | 0.91 |
| 6 | 500 | 50 | 2 | 0.6 | 5.02 | 5.88 | 6.95 | 0.33 |
| 7 | 500 | 150 | 2 | 0.6 | 4.17 | 4.89 | 5.72 | 0.32 |
| 8 | 500 | 200 | 2 | 0.6 | 3.52 | 4.19 | 4.98 | 0.35 |
| 9 | 500 | 250 | 0.5 | 0.6 | 5.39 | 8.13 | 12.19 | 0.84 |
| 10 | 500 | 250 | 1 | 0.6 | 2.61 | 4.51 | 7.49 | 1.08 |
| 11 | 500 | 250 | 4 | 0.6 | 1.95 | 3.45 | 5.87 | 1.13 |
| 12 | 500 | 250 | 2 | 0.3 | 4.10 | 4.86 | 5.74 | 0.34 |
| 13 | 500 | 250 | 2 | 0.4 | 2.60 | 4.34 | 6.94 | 1.00 |
| 14 | 500 | 250 | 2 | 0.5 | 3.61 | 4.33 | 5.10 | 0.34 |
| 15 | 500 | 250 | 2 | 0.75 | 3.43 | 4.06 | 4.88 | 0.36 |

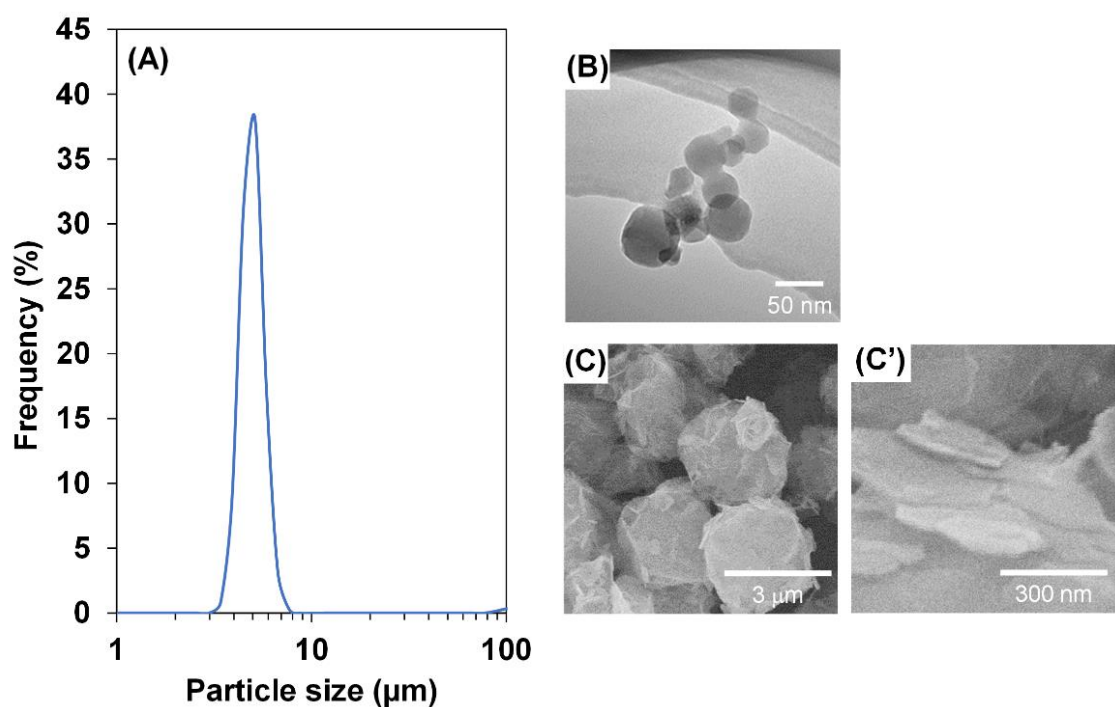[1] Inlet temperature was fixed at 150 °C for all the conditions.



**Figure 1.   Characterization of S-MgO(H$_2$O) particles. (A) Particle size distribution, (B) TEM image of the raw MgO nanoparticles (MgO50), (C) SEM image, and (C') its high magnification.**

In order to identify the origin of the plate-like texture, the feeding slurry with water as the dispersant before being spray-dried was analyzed. Figure 3A,A' show the SEM images of the dried slurry (MgO50($H_2O$)). A large number of plate-like particles, with a lateral dimension of less than 1 µm, was observed, confirming that the plate-like morphology appeared even before spray-drying. The XRD patterns of the raw materials MgO50 and MgO50($H_2O$) are shown in Figure 3B. As a matter of course, MgO50 only exhibited diffraction peaks characteristic of MgO, but in MgO50($H_2O$), the MgO peaks disappeared, and the peaks that can be attributed to $Mg(OH)_2$ appeared instead. It is plausible that the hydroxyl radicals generated by ultrasonication reacted with MgO to produce $Mg(OH)_2$. To avoid this undesirable phenomenon, methanol was used as a dispersant, instead of water, to prepare a feeding slurry (MgO50(MeOH)). The dried feeding slurry showed no plate-like particles in the SEM observation, and no diffraction peak derived from $Mg(OH)_2$ was observed by XRD (Figure 3B). Due to the difference in the physical properties between the dispersants, it became necessary to screen the spray-drying conditions for methanol as the dispersant (Table 2). Condition 6 in Table 2 was chosen as it resulted in spherical particles (Figure 3C,C') with a narrower size distribution compared to other investigated conditions. Thus, the obtained sample was named S-MgO. As shown in the XRD pattern of Figure 3B, no $Mg(OH)_2$-derived peaks were observed in

S-MgO. Thus, spherical-shaped secondary agglomerated MgO macroparticles, free from

Mg(OH)$_2$ contamination, could be obtained by using methanol as the dispersant.

**Table 2. Screening of spray-drying conditions for methanol dispersant.**

| Condition | Inlet temperature (°C) | Feed rate (mL h$^{-1}$) | Atomization air pressure (kPa) | Slurry concentration (g L$^{-1}$) | Blowing rate (m$^2$ min$^{-1}$) | $D_{10}$ (µm) | $D_{50}$ (µm) | $D_{90}$ (µm) | RSF |
|---|---|---|---|---|---|---|---|---|---|
| 1 | 90 | 500 | 250 | 2 | 0.6 | 1.99 | 3.78 | 6.85 | 1.29 |
| 2 | 110 | 500 | 250 | 2 | 0.6 | 1.77 | 3.20 | 5.70 | 1.23 |
| 3 | 110 | 500 | 200 | 2 | 0.6 | 1.77 | 3.35 | 6.08 | 1.29 |
| 4 | 110 | 500 | 200 | 4 | 0.6 | 1.75 | 3.05 | 5.09 | 1.09 |
| 5 | 140 | 500 | 250 | 2 | 0.6 | 1.67 | 3.01 | 5.28 | 1.20 |
| 6 | 160 | 800 | 200 | 4 | 0.3 | 3.93 | 4.58 | 5.37 | 0.31 |
| 7 | 160 | 800 | 270 | 4 | 0.3 | 4.04 | 4.72 | 5.52 | 0.32 |
| 8 | 160 | 800 | 200 | 10 | 0.3 | 3.25 | 3.88 | 4.61 | 0.35 |
| 9 | 160 | 800 | 200 | 30 | 0.3 | 3.86 | 4.48 | 5.22 | 0.30 |
| 10 | 160 | 800 | 200 | 60 | 0.3 | 3.98 | 4.71 | 5.62 | 0.35 |
| 11 | 180 | 800 | 200 | 4 | 0.3 | 3.65 | 5.65 | 8.69 | 0.89 |
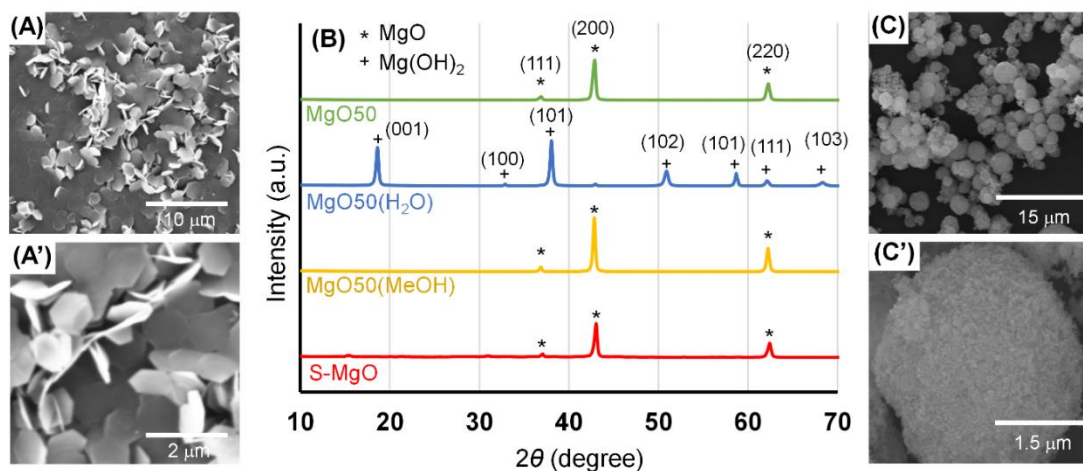
**Figure 3.** **Characterization of the MgO feeding slurries and the spray-dried particles. (A) SEM image of dried feeding slurry of MgO/water (MgO50(H₂O)) and (A') its high-magnification SEM image; (B) XRD patterns; (C) SEM image of the spray-dried MgO particles of which dispersion media is methanol (S-MgO) and (C') its high-magnification SEM image.**

Three catalyst samples were prepared by the TiCl$_4$ treatment of raw MgO50 nanoparticles, MgO50 nanoparticles dispersed by the PA surfactant treatment (PA-MgO50), and S-MgO spray-dried spherical macroparticles. These catalysts were named Cat50, PA-Cat50, and S-Cat, respectively. The results of the particle size distribution analysis in *n*-heptane, before and after the TiCl$_4$ treatment, are shown in Figure 4 and Table 3. MgO50 showed a broad particle size distribution centered at ca. 10 µm, with an RSF value of 1.12. After the TiCl$_4$ treatment of MgO50, another peak centered around 100 µm appeared, and the RSF value of the resultant catalyst (Cat50) significantly increased to 8.25. This is because the particles that were not well dispersed at the raw

material stage probably fused together when its surface converted to a $MgCl_2/TiCl_4$ catalyst overlayer by $TiCl_4$ treatment, which further inhibited dispersion. On the other hand, MgO50 treated with a surfactant (PA-MgO50) showed a much narrower particle size distribution (RSF = 0.49), and the average particle size ($D_{50}$ = 0.07 µm) is fairly close to the specification value of 50 nm of MgO50. The surfactant likely diminished the electrostatic interaction among the MgO nanoparticles, thereby enabling high dispersion of the particles in $n$-heptane [11]. Furthermore, the $TiCl_4$ treatment of PA-MgO50 hardly changed the particle size and distribution for PA-Cat50 ($D_{50}$ = 0.07 µm and RSF = 0.44), assuring that the original dispersion of PA-MgO50 particles in $n$-heptane prevailed after catalyst preparation. In contrast to the primary MgO particles, the secondary agglomerated macroparticles (S-MgO) showed a sharp and narrow particle size distribution without using a surfactant, exemplified by a smaller RSF value of 0.36. Also, both the $D_{50}$ and RSF remained nearly unaffected, even after the $TiCl_4$ treatment (change in $D_{50}$ = 4.84 to 4.98 µm, and change in RSF = 0.36 to 0.31, respectively). This surfactant-free dispersion was probably due to the decrease in the apparent surface area by aggregation, making the surface forces, such as the electrostatic interaction, less significant. Table 3 also contains the Ti loading of each catalyst sample. The relatively low Ti loading of Cat50 compared to industrial ZNCs (1–3 wt.%) can be attributed to the

fact that the size of the primary particles (50 nm) is larger than that of the industrial catalysts (2–10 nm). S-Cat had a comparable Ti loading to that of Cat50, which supports the fact that the secondary agglomerated macroparticles were successfully obtained while maintaining the properties of the primary particles. On the other hand, the relatively high Ti loading of PA-Cat50 (0.76 wt.%) is due to the coordination of additional $TiCl_4$ molecules with the ether group of the PA surfactant, as confirmed earlier by FT-IR investigation [11].
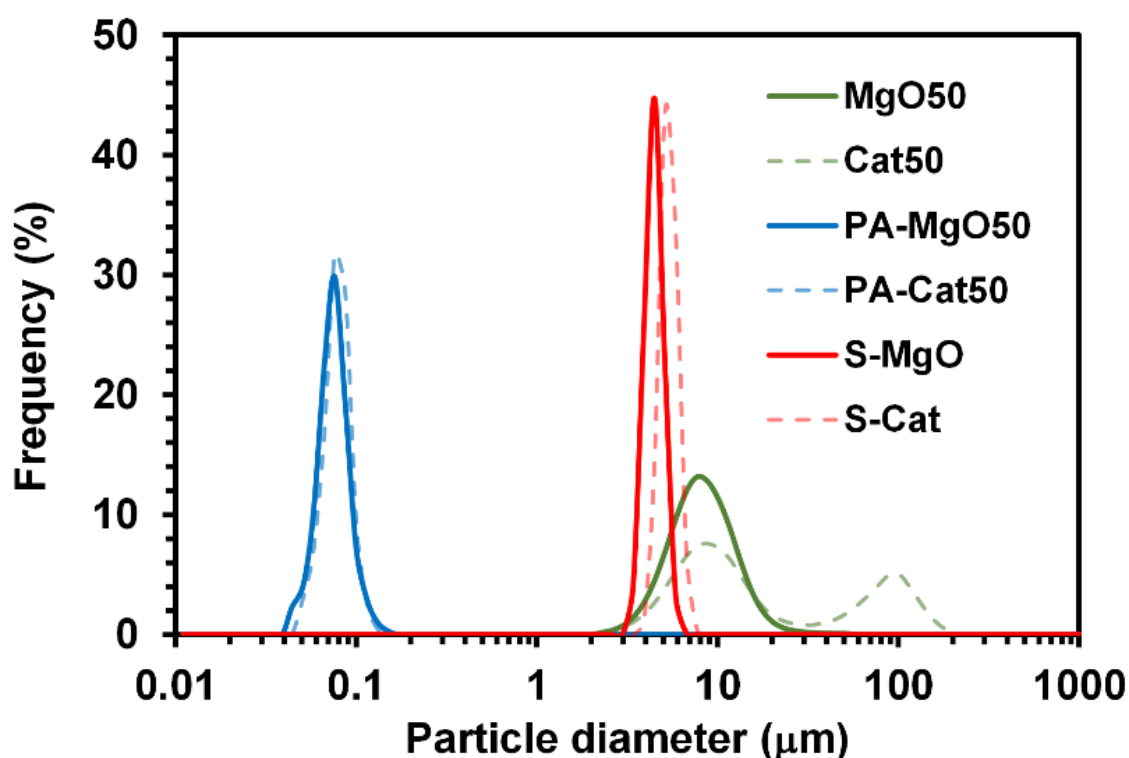


**Figure 4.  Particle size distribution of the three supports before and after TiCl₄ treatment, measured by light scattering experiment using *n*-heptane as the dispersant.**

**Table 3.    Summary of the particle size analysis of the support and catalyst samples.**

| Sample Name | $D_{10}$ (µm) | $D_{50}$ (µm) | $D_{90}$ (µm) | RSF | BET Surface Area $(m^2g^{-1})$ | Ti Cont. (wt.%) |
|---|---|---|---|---|---|---|
| MgO50 | 4.48 | 7.58 | 13.0 | 1.12 | 34.3 | |
| PA-MgO50 | 0.05 | 0.07 | 0.09 | 0.49 | | |
| S-MgO | 4.04 | 4.84 | 5.77 | 0.36 | 24.2 | |
| Cat50 | 5.02 | 11.3 | 98.3 | 8.25 | 33.5 | 0.47 |
| PA-Cat50 | 0.06 | 0.07 | 0.09 | 0.44 | 32.6 | 0.76 |
| S-Cat | 4.25 | 4.98 | 5.80 | 0.31 | 26.6 | 0.30 |

Figure 5A shows the $N_2$ adsorption/desorption isotherm of each support and catalyst sample. MgO50 exhibited almost no slope in the low-pressure region ($p/p_0 > 0.01$) of the adsorption isotherm, followed by a gradual increase in $N_2$ adsorption up to around $p/p_0 = 0.8$, and a sharp increase up to $p/p_0 = 1$. The absence of adsorption in the low-pressure region and no hysteresis together suggest that micropores ($\varphi < 2$ nm) and mesopores ($2 < \varphi < 50$ nm) were almost nonexistent in MgO50. The sharp rise in $N_2$ adsorption in the high-pressure region indicates the presence of macropores originated from the interparticle voids of the aggregated MgO nanoparticles. The BET-specific surface area of MgO50 was 34.3 $m^2\ g^{-1}$ (Table 1), close to the theoretical surface area (32.9 $m^2\ g^{-1}$) determined by assuming the MgO50 particle as a sphere with a diameter of 50 nm and a specific gravity of 3.65 $g\ ml^{-1}$. The isotherms of S-MgO were almost overlapped with those of MgO50, and the BET-specific surface area was comparable (24.2 $m^2\ g^{-1}$), suggesting that the interior structures of S-MgO correspond to the aggregation of MgO50

nanoparticles. The isotherms of the catalyst samples (Cat50, PA-Cat50, and S-Cat in

Figure 5B) were almost identical to each other and their respective supports. Moreover,

their BET-specific surface area was also similar to that of the supports, indicating that the

morphology of the primary particles was not significantly affected by the $TiCl_4$ treatment.
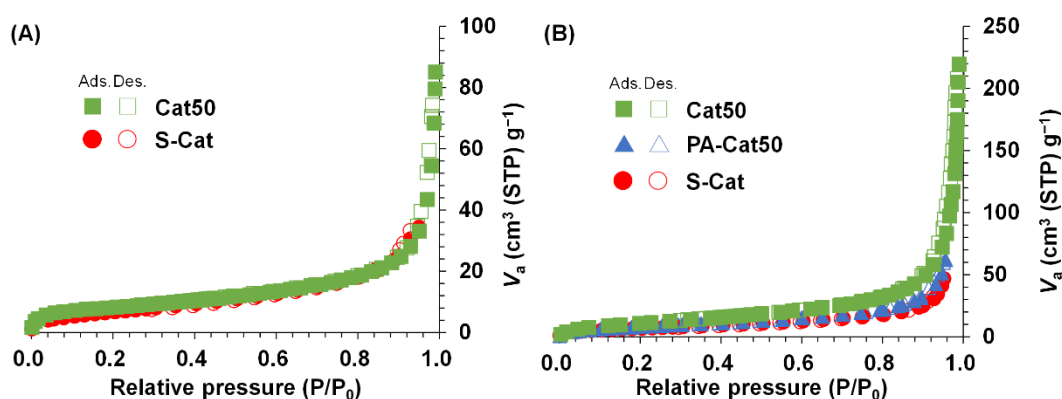


**Figure 5.** $N_2$ **adsorption/desorption isotherms of (A) support and (B) catalyst samples.**

The catalytic performance of S-Cat was first evaluated in the homo-polymerization of

both ethylene and propylene. To examine the effect of the multi-grain interior structure

on the polymerization kinetics, the fully dispersed catalyst PA-Cat50 was used as a

reference. The polymerization kinetic curves were drawn using the activity at a

polymerization time of 1–60 min (Figure 6 and Table 4). The activity of PA-Cat50 was

significantly lower than that of S-Cat (for ethylene, 6–7 times; for propylene, 16–30

times), plausibly due to the deactivation of a fraction of $TiCl_4$ molecules by complexation

with the PA surfactant, as described above [11]. On the other hand, they showed similar kinetic curves, i.e., the maximum activity was observed immediately after the polymerization started (1 min), and the activity reduced to half of its maximum value in about 30 min, and remained almost constant until the polymerization was stopped after 60 min. This kind of polymerization behavior is known as decay-type kinetics. Typical ZNCs, in which the exposure of buried Ti species occurs due to the fragmentation of catalyst particles during polymerization, show a build-up-type kinetic curve, i.e., the activity increases with time in the beginning, and remains stable for a prolonged duration. Thus the decay-type kinetics clearly indicates that the exposure of buried Ti species does not occur in the polymerization with both PA-Cat50 and S-Cat, and all Ti species on the catalysts were exposed from the beginning of polymerization. In addition, Figure 6 also suggests that macropores based on the aggregation of primary particles with the diameter of about 50 nm do not affect the diffusion of monomers, and thus do not affect the polymerization kinetics. These results, in turn, strongly support the fact that the presence of micropores and mesopores would be important to control polymerization kinetics.
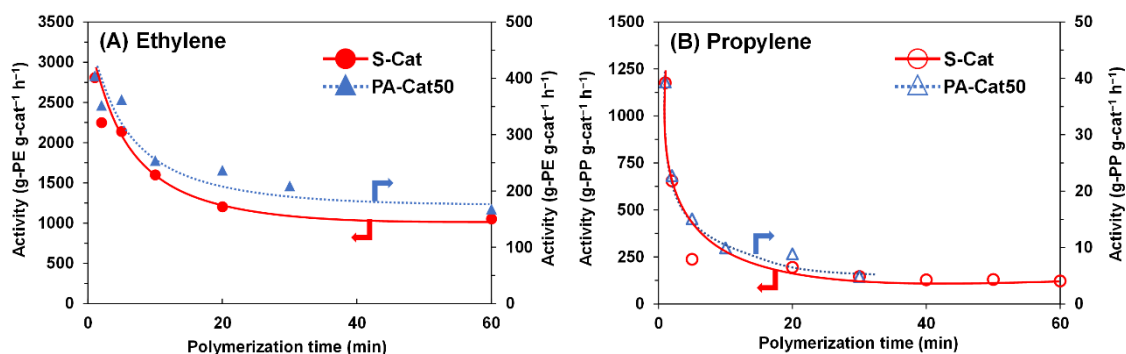
**Figure 6.** Polymerization kinetics of (A) ethylene and (B) propylene homo-polymerization with S-Cat and PA-Cat50.

**Table 4. Summary of ethylene and propylene polymerization results.**

| | Polymerization Time (min) | | | | | | | | |
|---|---|---|---|---|---|---|---|---|---|
| | 1 | 2 | 5 | 10 | 20 | 30 | 40 | 50 | 60 |
| Ethylene polymerization activity (g-PE g-cat$^{-1}$ h$^{-1}$) | | | | | | | | | |
| S-Cat | 2809 | 2249 | 2139 | 1599 | | 1539 | | | 1051 |
| PA-Cat50 | 404 | 352 | 362 | 254 | 237 | 209 | | | 168 |
| Propylene polymerization activity (g-PP g-cat$^{-1}$ h$^{-1}$) | | | | | | | | | |
| S-Cat | 1176 | 654 | 237 | | 194 | 146 | 129 | 130 | 122 |
| PA-Cat50 | 39 | 23 | 15 | 10 | 9 | 5 | | | |

The SEM images of the obtained polymer particles are shown in Figure 7. Since the fragmentation of catalyst particles on a typical ZNC occurs within a few seconds to a minute, here, we compare the polymer particles formed at the polymerization time of 1 min (early stage of the polymerization) and 30 min (when the polymer particle is expected to be almost fully grown). Each sample is expressed as xx-yyzz (xx: catalyst name, yy: polymer name, zz: polymerization time in min). It is found that PA-Cat50-PE1 (Figure 7C,C') is completely formless. Extending the polymerization time gave no significant

47

difference in the morphology of the polymer particles made by PA-Cat50 (PA-Cat50-PE30, Figure 7D,D'). This is probably due to the fact that the formation of the polymer diluted the PA surfactant, and, as a result, the catalyst particles could no longer maintain the monodispersity. A similar morphology is observed for the PP particles made by PA-Cat50 (i.e., PA-Cat50-PP1,30: Figure 7G,G', H,H'). On the other hand, the polymer particles synthesized by S-Cat (i.e., S-Cat-PE1,30, S-Cat-PP1,30: Figure 7A,A', B,B', E,E', F,F') mimicked the spherical morphology of the catalyst macroparticles plausibly, due to occurrence of the fragmentation process. In order to confirm the dissociation of MgO nanoparticles during polymerization, the cross-section of polymer particles formed at 1 min polymerization time was observed by SEM-EDX (Figure 8). In both S-Cat-PE1 and S-Cat-PP1, the Mg, Cl, O, Al, and Ti elements were almost uniformly dispersed on the surface of the cross-section, indicating that the $MgO/MgCl_2/TiCl_4$ core–shell catalyst particles were dissociated from each other at the polymerization time of 1 min. On the other hand, fibril morphology was observed on the surface of the polymer particles produced by S-Cat (Figure 7A', B', F'). This fibrous morphology has hardly been reported for ZN catalysts, but it is probably formed by hydraulic extrusion of the polymer generated inside the pores. The same fibril morphology was observed in PE produced with a $MgO/MgCl_2/TiCl_4$ core–shell catalyst, without spray-drying [10]. The absence of

PE fibrils in PA-Cat50 suggests that the aggregation of primary particles in S-Cat is somehow related to the fibril structure, but the detailed mechanism is still unclear.

The copolymerization with 1-hexene was performed for both ethylene and propylene. The results for S-Cat and PA-Cat50 are summarized in Tables 5 and 6, respectively. The ethylene polymerization performance of Cat50 has already been reported in the previous paper [10]. Since the polymerization is carried out using $n$-heptane as a solvent, low-crystalline components dissolved in the solvent. After the separation of polymer particles, the remining filtrate was casted into an excess amount of acetone to solidify and collect the low-crystalline component, and the activity was calculated using the sum of the insoluble and soluble polymers. It has long been known that the addition of a small amount of comonomer significantly increases the activity compared to homo-polymerization. This phenomenon is often referred to as the comonomer effect. The mechanism is still under discussion, and various reports have been made, even in recent years. The possible origins proposed so far are (1) a reduction in the barrier effect of the generated polymer [13,14]; (2) activation of dormant sites [15,16]; and (3) enhancement of catalyst fragmentation, to expose Ti species that is not used for homo-polymerization [17–19]. The activity enhancement by comonomer is typically 2–10 times in normal ZNC [17,20].
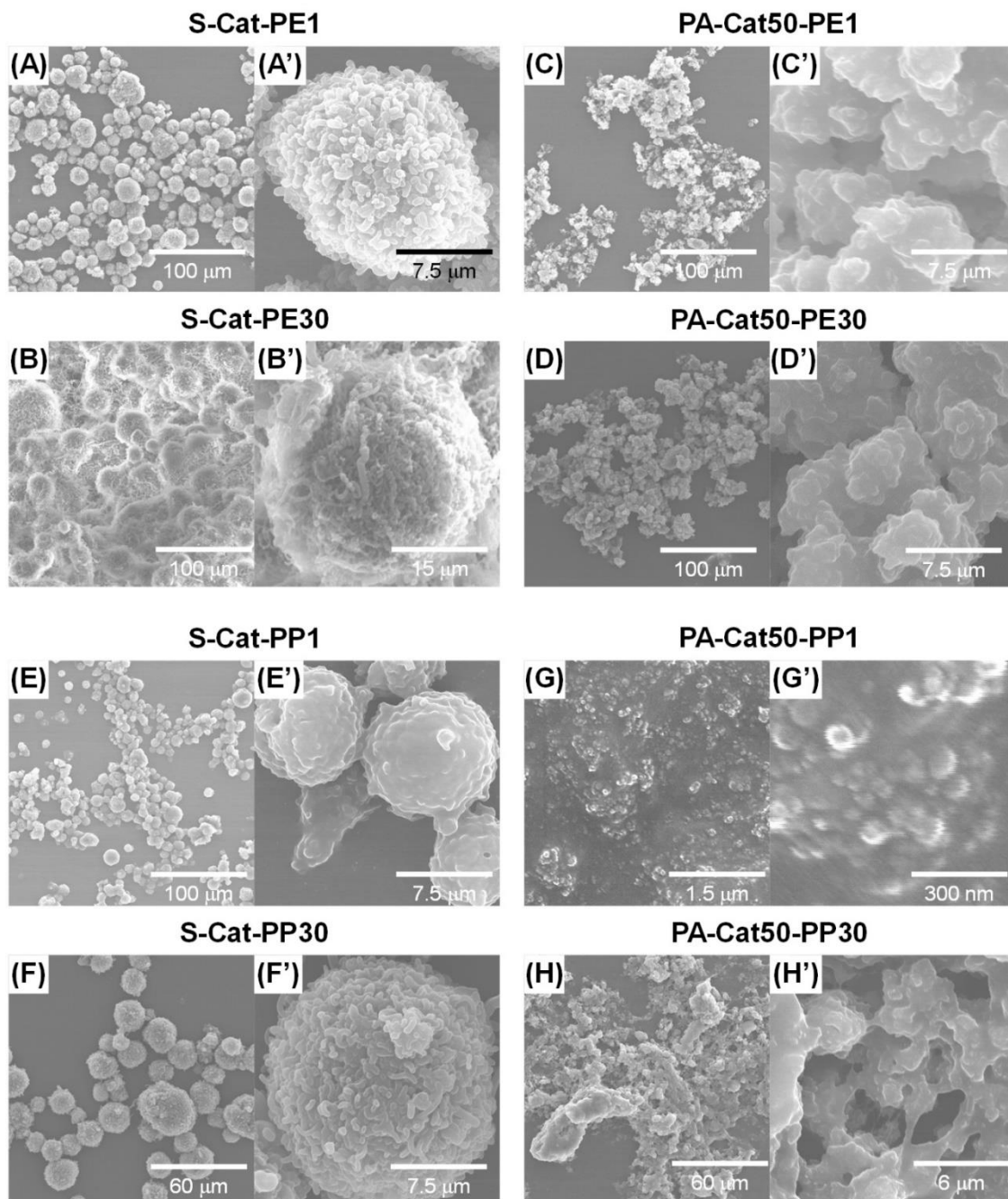
**Figure 7.** **SEM images of polymer particles obtained with S-Cat and PA-Cat50. The sample name corresponds to the catalyst name and polymerization conditions as xx-yyzz (xx: catalyst name, yy: polymer name, zz: polymerization time in min). PE obtained with S-Cat for (A) 1 min and (B) 30 min. PE obtained with PA-Cat50 for (C) 1 min and (D) 30 min. PP obtained with S-Cat for (E) 1 min and (F) 30 min. PE obtained with PA-Cat50 for (G) 1 min and (H) 30 min. (A'-H') high-**

**S-Cat-PE1**  **S-Cat-PP1**
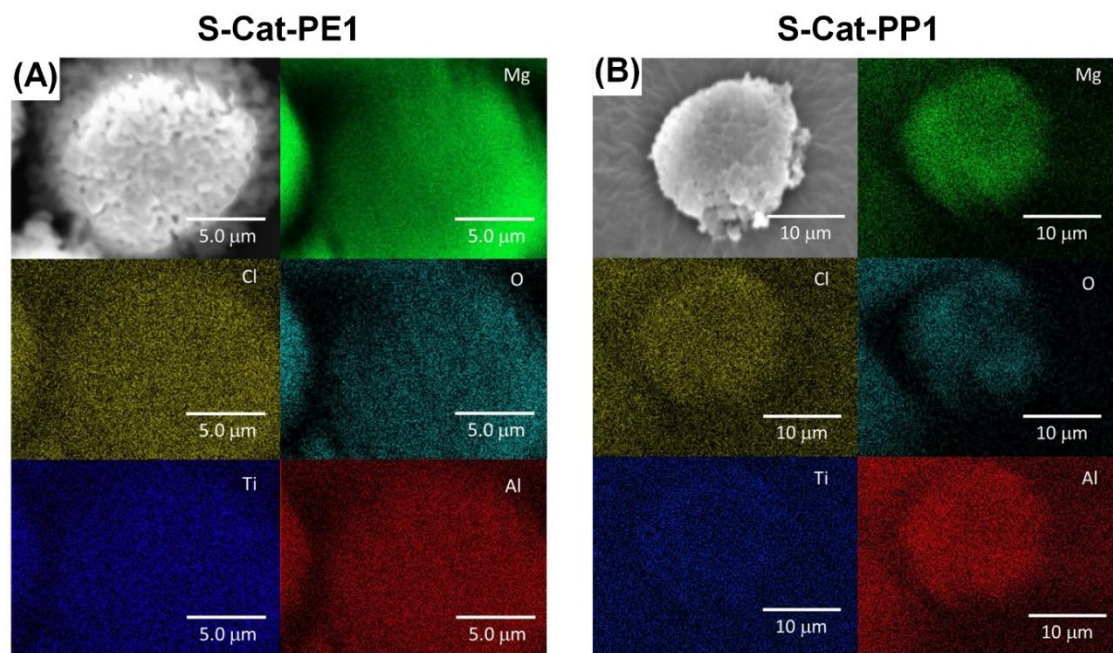
magnification images of A-H.

**Figure 8.** **SEM-EDX images of cross-section of (A) PE and (B) PP particles obtained with S-Cat at short time polymerization (1 min).**

**Table 5. 1-Hexene copolymerization with ethylene.**

| Catalyst | 1-Hexene (mol L$^{-1}$) | Polymer Yield (g-pol g-cat$^{-1}$) | | Activity (g-pol g-cat$^{-1}$ h$^{-1}$) | Activity (kg-pol mmol-Ti$^{-1}$ h$^{-1}$) | Comonomer Effect [1] | Hexene Content (mol%) [2] | |
|---|---|---|---|---|---|---|---|---|
| | | Insoluble | Soluble | | | | Insoluble | Soluble |
| S-Cat | 0 | 803 | trace | 1607 | 25 | | n.a. | n.a. |
| | 0.4 | 1421 | trace | 2842 | 45 | 1.8 | 0.01 | |
| | 0.8 | 1618 | 11.6 | 3259 | 52 | 2.0 | 0.02 | 10.0 |
| | 1.2 | 1513 | 44.1 | 3115 | 50 | 1.9 | 0.03 | |
| | 2.4 | 1247 | 384 | 3262 | 52 | 2.0 | 0.07 | 15.5 |
| PA-Cat50 | 0 | 112 | trace | 223 | 3.6 | | n.a. | n.a. |
| | 0.4 | 92 | trace | 184 | 2.9 | 0.8 | 0.01 | |
| | 0.8 | 88 | trace | 177 | 2.8 | 0.8 | 0.02 | |
| | 1.2 | 103 | trace | 205 | 3.3 | 0.9 | 0.02 | |
| | 2.4 | 92 | trace | 183 | 2.9 | 0.8 | 0.07 | |

[1] Calculated by activity of copolymerization with 1-hexene/activity of homo-polymerization. [2] n.a.: not applicable, blanks: not determined, n.d.: not detected.

**Table 6.   1-Hexene copolymerization with propylene.**

| Catalyst | 1-Hexene (mol L−1) | Polymer Yield (g-pol g-cat⁻¹) | | Activity (g-pol g-cat⁻¹ h⁻¹) | Activity (kg-pol mol-Ti⁻¹ h⁻¹) | Comonomer Effect [1] | Hexene content (mol%) [2] | | mmmm of PP Unit (mol%) [2] | |
|---|---|---|---|---|---|---|---|---|---|---|
| | | Insoluble | Soluble | | | | Insoluble | Soluble | Insoluble | Soluble |
| **S-Cat** | 0 | 38.8 | 8 | 94 | 1496 | | n.a. | n.a. | 79.8 | |
| | 0.4 | 36.7 | 46 | 164 | 2624 | 1.8 | 2.7 | 5.1 | 84.0 | 34.7 |
| | 0.8 | 34.1 | 52 | 173 | 2760 | 1.8 | | | | |
| | 1.2 | 27.5 | 99 | 254 | 4051 | 2.7 | | | | |
| | 2.4 | 14.8 | 103 | 236 | 3762 | 2.5 | 8.1 | 26.9 | 84.2 | 46.2 |
| **PA-Cat50** | 0 | 1.72 | trace | 3.4 | 42 | | n.a. | n.a. | 84.6 | |
| | 0.4 | 2.45 | trace | 4.9 | 60 | 1.4 | n.d. | | 86.8 | |
| | 0.8 | 2.08 | trace | 4.2 | 51 | 1.2 | | | | |
| | 1.2 | 1.30 | trace | 2.6 | 32 | 0.8 | | | | |
| | 2.4 | 1.14 | trace | 2.3 | 28 | 0.7 | n.d. | | 87.7 | |

[1] Calculated by activity of copolymerization with 1-hexene/activity of homo-polymerization. [2] n.a.: not applicable, blanks: not determined, n.d.: not detected.

As shown in Tables 5 and 6, the activity was increased by the presence of 1-hexene in both the ethylene and propylene polymerization using S-Cat. In the case of ethylene, the activity increased about two times, regardless of the amount of 1-hexene, and in copolymerization with propylene, the activity increased about 2.5 to 3 times with increasing the amount of 1-hexene. The content of 1-hexene in the copolymer samples also increased with the increase in 1-hexene in the reaction system. In particular, the 1-hexene content of the heptane-soluble component polymer changed significantly, suggesting that the insertion of 1-hexene into the polymer chain reduced the polymer crystallinity. It is interesting that such a sufficient comonomer effect was observed for S-Cat, even though its catalyst overlayer was fully opened from the beginning, in terms of fragmentation. This suggests that diffusion inhibition by the polymer film (barrier effect)

also works at the level of the primary catalyst particles. On the other hand, when PA-Cat50 was used, no comonomer effect was observed for both ethylene and propylene. The 1-hexene content in the copolymer increased slightly with the amount of 1-hexene introduced. In propylene/1-hexene copolymer samples, the incorporation of 1-hexene was not detected. It is considered that 1-hexene was hardly inserted into the polymer, due to the presence of the surfactant, and thus the comonomer effect did not appear.

The content of the *mmmm* sequence of PP, obtained by S-Cat, was 79.8 mol%, which is higher than that of PP obtained by internal/external donor-free $MgCl_2$-supported ZNC [9]. The removal of the soluble component, and the use of TIBA as a co-catalyst probably contributed to it. The reason why 1-hexene improved the stereoregularity of the insoluble component was thought to be because the crystallinity of the slightly lower stereoregular PP in the insoluble component was decreased by the introduction of 1-hexene and removed as a soluble component. The stereoregularity of the soluble component seems to increase with increasing the amount of 1-hexene, but this is probably because 1-hexane is introduced into the originally highly stereoregular PP, thus increasing the ratio of the soluble component. The stereoregularity of the whole polymer is estimated from the yields of insoluble and soluble components (($\text{Yield}_{insol} \times mmmm_{insol} + \text{Yield}sol \times mmmm_{sol}$)/($\text{Yield}_{insol} + \text{Yield}_{sol}$)): 56.6 mol% for 0.4 mol $L^{-1}$ and 51.0 mol% for 2.4 mol

$L^{-1}$, which seems consistent with the trend of the comonomer effect. The fact that the stereoregularity of the PP obtained with PA-Cat50 is slightly higher than that of S-Cat can be attributed to the fact that the surfactant affects the bulkiness of the vicinity of the active site. The stereoregularity was almost unchanged by introducing 1-hexene, which is consistent with the fact that 1-hexene was hardly incorporated.

## *2.4. Conclusions*

In summary and conclusion, spherical macroparticles with a narrow particle size distribution were obtained by the spray-drying of MgO nanoparticles (50 nm in di-ameter), using methanol as a dispersant. The subsequent $TiCl_4$ treatment allowed us to realize the bottom-up preparation of the multi-grained $MgO/MgCl_2/TiCl_4$ core–shell catalyst (S-Cat). The catalyst has no micropores and mesopores, but it possesses macropores derived from the interparticle voids among MgO nanoparticles with a diameter of 50 nm. S-Cat showed decay-type kinetic curves in the homo-polymerization of both ethylene and propylene, i.e., the catalyst displayed the highest activity at the early stage of polymerization, and then its activity dropped to a certain level, which remained constant until the polymerization was stopped. These polymerization behaviors were similar to that of a monodispersed $MgO/MgCl_2/TiCl_4$ core–shell catalyst treated with a surfactant (PA-Cat50), suggesting that macropores never influenced the diffusion of the cocatalyst and the monomer. Thus, all the catalyst overlayers in S-Cat were open for a polymerization reaction from the beginning. These facts, in turn, indicate that the micropores and mesopores are deeply involved in the fragmentation and build-up kinetics. Even when using S-Cat with fully opened sur-faces, the degrees of activation (comonomer effect) by introducing 1-hexene in both ethylene and propylene copolymerization were comparable

to that of general hetero-geneous Ziegler–Natta catalysts. This fact suggests that the diffusion inhibition effect of the polymer layers is effective, even at the level of the primary catalyst particles. As described above, the multi-grained $MgO/MgCl_2/TiCl_4$ core–shell catalyst was shown to be useful for obtaining insights into the structure–performance relationship of ZNCs, with respect to their interior structures. In the following studies, it is expected that quantitative discussions will be available, by controlling the interior structure by in-tentionally changing the size of the primary particles, etc., which would give us clearer insights into the structure–performance relationship of $MgCl_2$-supported ZNCs.

## Reference

[1] F. Machado, E. L. Lima, J. C. Pinto, T. F. McKenna, *Eur. Polym. J.* **2008**, 44, 1130–1139.

[2] T. Wada, A. Thakur, P. Chammingkwan, M. Terano, T. Taniike, A. Piovano, E. Groppo, *Catalysts* **2020**, *10*, 1089–1102.

[3] M. A. Ferrero, M. G. Chiovetta, *Polym. Eng. Sci.* **1987**, 27, 1436–1447.

[4] M. A. Ferrero, M. G. Chiovetta, *Polym. Eng. Sci.* **1987**, 27, 1448–1460.

[5] M. A. Ferrero, M. G. Chiovetta, *Polym. Eng. Sci.* **1991**, 31, 886–903.

[6] P. Umare, R. Antony, K. Gopalakrishnan, G. Tembe, B. Trivedi, *J. Mol. Catal. A Chem.* **2005**, 242, 141–150.

[7] T. Taniike, T. Funako, M. Terano, *J. Catal.* **2014**, 311, 33–40.

[8] L. Xu, Y. Huang, J. Xu, X Ji, Z. Li, *RSC Adv.* **2014**, 4, 1512–1520.

[9] P. Chammingkwan, V. Q. Thang, M. Terano, T. Taniike, *Top. Catal.* **2014**, 57, 911–917.

[10] Y. Bando, P. Chammingkwan, M. Terano, T. Taniike, *Macromol. Chm. Phys.* **2018**, 219, 1800011.

[11] P. Chammingkwan, Y. Bando, M. Terano, T. Taniike, *Front. Chem.* **2018**, 6, 524.

[12] P. Chammingkwan, Y. Bando, L. T. T. Mai, T. Wada, A. Thakur, M. Terano, L.

Sinthusai, T. Taniike, *Ind. Eng. Chem. Res.* **2021**, 60, 2818–2827.

[13] A. Muñoz-Escalona, H. Garcia, A. Albornoz, *J. Appl. Polym. Sci.* **1987**, 34, 977–988.

[14] K. Soga, H. Yanagihara, D. H. Lee, *Macromol. Chem.* **1989**, 190, 995–1006.

[15] Y. V. Kissin, R. I. Mink, T. E. Nowlin, *J. Polym. Sci. Part A Polym. Chem.* **1999**, 37, 4255–4272.

[16] Y. V. Kissin, R. I. Mink, T. E. Nowlin, A. J. Brandolini, *Top. Catal.* **1999**, 7, 69–88.

[17] P. J. T. Tait, I. G. Berry, *Surf. Sci. Catal.* **1994**, 89, 55–72.

[18] M. H. Nejad, P. Ferrari, G. Pennini, G. Cecchin, *J. Appl. Polym. Sci.* **2008**, 108, 3388–3402.

[19] T. Xu, H. Yagn, Z. Fu, Z. Fan, *J. Organomet. Chem.* **2015**, 798, 328–334.

[20] L. Zhang, Z. Fan, Z. Fu, *Chin. J. Polym. Sci.* **2008**, 26, 605.

[21] J. C. Randall, *J. Macromol. Sci. Part C* **1989**, 29, 201–317.

[22] Y. V. Kissin, A. J. Brandolini, *Macromolecules* **1991**, 24, 2632–2633.

[23] V. Busico, R. Cipullo, *Prog. Polym. Sci.* **2001**, 26, 443–533.

Chapter 3

# *Bottom-Up Synthesized Ziegler-Natta Catalyst for Ultra-High Molecular Weight Polyethylene*

## *3.1.  Introduction*

The physical properties of polyethylene (PE) depend largely on the molecular weight, molecular weight distribution, and the amount and length of side chains. High-density polyethylene (HDPE), which is widely used as a commodity resin, has a linear structure, and its molecular weight is generally about 2 to $5 \times 10^5$ g mol$^{-1}$. PE with even higher molecular weight ($> 1$ to $1.5 \times 10^6$ g mol$^{-1}$) is termed as ultra-high molecular weight polyethylene (UHMWPE) [1], and has better mechanical properties such as tensile strength, elastic modulus, abrasion resistance, and self-lubrication, while maintaining the advantages of PE materials such as high corrosion resistance and chemical resistance and hence it is in demand for applications in harsh environments such as artificial joints, lightweight high-strength fibers, tapes, and metal substitute ropes, etc. Due to the extremely high molecular weight, the melt viscosity of UHMWPE is crucially high as a result of the significant entanglement of polymer chains. Therefore, although it is a thermoplastic resin, molding methods based on the low of molten polymer (extrusion molding, hollow molding, extrusion molding, injection molding, etc.) cannot be applied. Therefore, compression molding is mainly applied. In order to carry out compression molding, fine particles of UHMWPE are required as raw materials. In addition to the molded products, the fine particles itself are also used as functional materials. Particles

with a very small diameter (>70 μm), termed as microfine grade, are used as additives for resins, paints, and greases, taking advantage of their self-lubricating properties, and as raw materials for sintered micro-filters. In all of these applications, the particle size, size distribution, and morphology of UHMWPE particles are closely related to the molding processability, quality, and function of the processed product, so it is important to control these factors.

A number of attempts to prepare UHMWPE microparticles have been reported, and they can be broadly classified into two categories: the method of obtaining UHMWPE polymerization powder using very fine catalyst particles and the method of processing UHMWPE into microparticles. Most of UHMWPE is synthesized by heterogeneous Ziegler-Natta (ZN) catalysts. Since the morphology of the polymer particles mimics the shape of the catalyst particles (replica phenomena) [2], the particle size and morphology of the polymerized powder can be controlled through those of catalyst particles. When both the catalyst particles and the resultant UHMWPE particles are spherical, the particle size of the polymerized powder is proportional to $Y^{1/3} D_{\mathrm{Cat}}$. where $Y$ and $D_{\mathrm{Cat}}$ are the polymer yield per catalyst and catalyst particle size, respectively [3]. The particle size can also be reduced by limiting the polymer yield $Y$, but this is not realistic because its impact is 1/3 power, and the productivity is sacrificed. Therefore, it is fundamentally important

to obtain catalysts with small particle size; however, it is not easy, especially with controlled morphology. In general, spherical ZN catalysts have a particle size of 20-few tens μm, which is too large to obtain ultrafine grade UHMWPE particles of less than 70 μm. Crushing the catalyst particles to make them finer has been proposed [4], but it remains a problem in terms of morphology control. It has been reported that spherical catalyst particles with a diameter of about 1 μm can be synthesized by dropping a solution of $MgCl_2$ into $TiCl_4$ to solidify catalyst particles, which is one of the success stories of commercializing ultrafine grade UHMWPE particle with a diameter of about 10 μm [5,6]. On the other hand, the process is rather complicated and requires multiple $TiCl_4$ treatment and washing steps to remove coordinating agents, etc.

Chammingkwan et al. synthesized a ZN catalyst with extremely small particle size (ca. 50 nm) from MgO nanoparticles as a raw material, which enable to produce submicron grade UHMWPE particles with a diameter of 1-2 μm [3]. MgO nanoparticle modified with a surfactant was dispersed in $TiCl_4$ at sufficiently high temperature, converting the outer surface of the nanoparticle into thin $MgCl_2/TiCl_4$ catalyst layer (the thickness is ca. 1-2 nm). Thus core-shell $MgO/MgCl_2/TiCl_4$ catalyst can be prepared in one step [3]. This method has the following advantages: (1) the morphology of the catalyst particles mimics that of the raw MgO nanoparticles, thus eliminating the morphology control processes,

(2) the Cl content is lower than that of other $MgCl_2$-supported ZN catalysts and hence the obtained polymer would have less health concerns, which is more suitable to implants such as artificial joints, (3) no ligands such as alcohols are present, thus eliminating the need for their removal processes, and (4) fewer processes are required. In addition, the UHMWPE microparticles obtained in this way showed low temperature fusing property due to the small particle size. On the other hand, due to the extremely small diameter of the catalyst, microfine grade particles, which are expected to have wider application, could not be obtained, and the resulting UHMWPE particles had an irregular shape.

We previously prepared MgO nanoparticles into spherical secondary agglomerates with a narrow size distribution and a particle size of about 4-5 μm by using a spray dryer and chlorinated them with $TiCl_4$ to prepare $MgO/MgCl_2/TiCl_4$ core-shell catalysts [7]. In this study, the spherical secondary particle catalysts obtained in this way were used to synthesize spherical ultrafine grade UHMWPE particles.

## 3.2. Experimental

### 3.2.1. Materials

MgO nanoparticles with the mean particle size of 50 nm (MgO50), methanol, and titanium tetrachloride ($TiCl_4$) were purchased from FUJIFILM Wako Pure Chemical Co., Ltd. and used as received. *n*-Heptane (Wako Pure Chemical Co., Ltd.) was used after dehydration by $N_2$ bubbling with molecular sieve 4A for 2 h. Ethylene of polymerization grade (Sumitomo Seika Chemicals Co., Ltd.) was used as received. 1-Hexene (purity > 97 %, Sigma-Aldrich Co. LLC) was used after dehydration by $N_2$ bubbling for 2 h in the presence of molecular sieve 4A. Triethylaluminium (TEA) donated by Tosoh Finechem Corp. was used after diluting to 1 mol $L^{-1}$ in heptane.

### 3.2.2. Spray-Drying of MgO nanoparticles

Pristine MgO nanoparticles (MgO50) were dispersed methanol by means of ultrasonication for 6 h to prepare a feeding slurry. The feeding slurry was introduced into the atomizer by a peristaltic pump and sprayed into the main chamber by compressed air. The sprayed droplets were dried by hot air in the main chamber where extremely large particles fell into the separation container, and the rest were carried over to the cyclone. Particles of a certain size were collected as a spray-dried product (denoted as S-MgO50-

XX, XX indicates the MgO slurry concentration fed to the spray-dryer) by centrifugal force, and fine particles were flown out to the exhaust line. The parameters for spray drying are feeding slurry concentration, feeding rate, inlet temperature, atomization air pressure, and blowing rate.

### 3.2.3. Catalyst Synthesis

0.5 g of S-MgO-XX was heated at 130 °C under $N_2$ flow for 6 h to remove physisorbed water before treating with 30 mL of $TiCl_4$ at the reflux temperature for 2 h. The obtained product (denoted as S-Cat50-XX, XX indicates the MgO slurry concentration fed to the spray-dryer) was repetitively washed with heptane and stored as a slurry in heptane under $N_2$.

### 3.2.4. Ethylene polymerization

Ethylene polymerization was carried out with a 1 L stainless steel autoclave equipped with a mechanical stirrer. After sufficient $N_2$ replacement in the autolcave, 500 mL of *n*-heptane and TEA were introduced to the reactor and then saturated with 0.8 MPa of ethylene at 70 °C for 30 min. Afterwards, c.a. 10 mg of a catalyst was charged to the reactor to initiate polymerization. The polymerization was carried out at a stirring speed of 750 rpm at a constant pressure and temperature for 2 hours.The obtained polymer was

filtered and dried in vacuum at 60 °C for 6 h.

### 3.2.5. Characterization

Particle morphological characteristics of catalyst particles and polymer particles were studied with scanning electron microscopy (SEM, Hitachi S-4100) performed at an accelerating voltage of 20 kV. Before the measurements, particles were subjected to Pt sputtering for 90 s.

The particle size distribution profiles of support and catalyst samples were acquired from a light scattering (Horiba Partica LA-950V2). The measurements were done in a suspension from using *n*-heptane as a medium unless stated. The particle size was expressed as D10, D50, and D90, which corresponded to the particle size at 10, 50, and 90% of the cumulative volume distribution. A relative span factor (RSF) was calculated based on Equation (1):

$$\text{RSF} = \frac{D_{90} - D_{10}}{D_{50}} \qquad (1)$$

Nitrogen adsorption and desorption isotherms at 77 K were acquired on a BELSORP-max instrument (BEL JAPAN, INC.). C.a. 20-50 mg of catalyst powder in a pyrex tube

with a rubber cap was outgassed at 80 °C over 2 h in vacuo, prior to the measurement.

The viscosity-average molecular weight ($M_v$) of a polymer sample was determined based on an ASTM D4020. The relative viscosity of a polymer solution was acquired using an electromagnetically spinning viscometer (EMS, Kyoto Electronics Manufacturing, EMS-100). A polymer sample was dissolved in decahydronaphthalene (20 mg dL$^{-1}$) under heating at 150 °C. Then, 300 μL of the polymer solution and an aluminum ball was transferred to a vial. The viscosity was measured at 135 °C based on the frustrated rotation of the aluminum ball in the solution. The relative viscosity ($\eta_{rel}$), specific viscosity ($\eta_{sp}$), intrinsic viscosity ($[\eta]$), and viscometric average molecular weight ($M_v$) were derived according to Equations (2)-(5), respectively,

$$\eta_{rel} = \frac{\eta_{solution}}{\eta_{solvent}} \qquad (2),$$

$$\eta_{sp} = \eta_{rel} - 1 \qquad (3),$$

$$[\eta] = \frac{\sqrt{\eta_{sp} - 2 \ln \eta_{rel}}}{C} \qquad (4),$$

$$M_v = 5.34 \times 10^4 [\eta]^{1.37} \qquad (5),$$

where $C$ is the polymer concentration in the solution (g dL$^{-1}$).

The melting temperature and crystallization temperature of polymer samples were obtained by a differential scanning calorimeter (DSC, Mettler Toledo DSC 822). The resulting reactor powder was heated to 180 °C under N2 flow at a heating rate of 10 °C min$^{-1}$. The melting temperature of polymer samples for the nascent form was determined from the melting endotherm peak in the first heat cycle. After keeping temperature at 180 °C for 10 min, the polymer sample was cooled down to 50 °C at the cooling rate of 10 °C min$^{-1}$ to determine non-isothermal crystallization temperature. Afterwards, the second heat cycle was applied at the heating rate of 10 °C min$^{-1}$ to obtain the melting temperature of melt-crystallized form.

For the specimen preparation, compression molding was used to prepare a 5 × 5 cm polymer film. A certain amount of reactor polymer powder was filled into an aluminum mold set between two thin plates. The sample pressed with a contact pressure at room temperature for 5 min. Thereafter, the temperature was raised to 120 °C and held for 6 minutes. Then, the total pressure of 20 MPa was applied for another 5 minutes. The obtained specimen was cooled to room temperature.

## *3.3. Result and Discussion*

To prepare the secondary agglomerated particles of MgO nanoparticles, spray drying was carried out under the conditions shown in Table 1. The diameters of the secondary agglomerated particles were about 3-5 μm. The RSF value, which is an index of the breadth of the particle size distribution, was as small as about 0.3 for all the samples, which demonstrates that uniform secondary particles could be obtained by spray drying. In the spray dryer, the slurry of MgO nanoparticles is sprayed into the main chamber by compressed air, and the secondary agglomerated particles are produced by evaporation of solvent from the droplets. Therefore, it is probably possible to control the BD and the particle size of the secondary particles by changing the evaporation rate of the solvent through the inlet temperature, the size of the droplets by changing the intensity of the atomization air pressure, and the amount of MgO nanoparticles in the droplets by changing the concentration of the feeding slurry. However, there was no systematic change in the properties of the secondary particles by varying the inlet temperature and atomization air pressure. This well reflects the fact that the atomization efficiency of droplets is largely governed by viscosity and surface tension [8]. On the other hand, as the feeding slurry was denser, the particle size increased and BD also slightly increased (Table 1, samples 1, 5, 6, and 7). The relationship between feeding slurry concentration

and sphere volume calculated from the particle size is shown in Figure 2. The particle

size increased uniformly with increasing Feeding slurry concentration.

**Table 1. Condition of spray drying and characterization of spray MgO samples**

| Sample name | Spray drying condition | | | Sample property | | | | |
| --- | --- | --- | --- | --- | --- | --- | --- | --- |
| | Inlet temperature (°C) | Atomization air pressure (×10 kPa) | Feeding slurry concentration (g L$^{-1}$) | $D_{10}$ (mm) | $D_{50}$ (mm) | $D_{90}$ (mm) | RSF | Bulk density[1] (g cm$^{-3}$) |
| Sample 1 | 160 | 20 | 4 | 3.41 | 3.97 | 4.69 | 0.32 | 0.17 ± 0.002 |
| Sample 2 | 80 | 20 | 4 | 3.76 | 4.40 | 5.11 | 0.31 | 0.13 ± 0.002 |
| Sample 3 | 120 | 20 | 4 | 2.65 | 3.07 | 3.52 | 0.28 | 0.13 ± 0.006 |
| Sample 4 | 160 | 10 | 4 | 3.15 | 3.68 | 4.30 | 0.31 | 0.13 ± 0.003 |
| Sample 5 | 160 | 20 | 40 | 3.51 | 4.12 | 4.86 | 0.33 | 0.18 ± 0.003 |
| Sample 6 | 160 | 20 | 80 | 3.76 | 4.34 | 5.03 | 0.29 | 0.21 ± 0.011 |
| Sample 7 | 160 | 20 | 160 | 3.97 | 4.67 | 5.75 | 0.37 | 0.21 ± 0.007 |

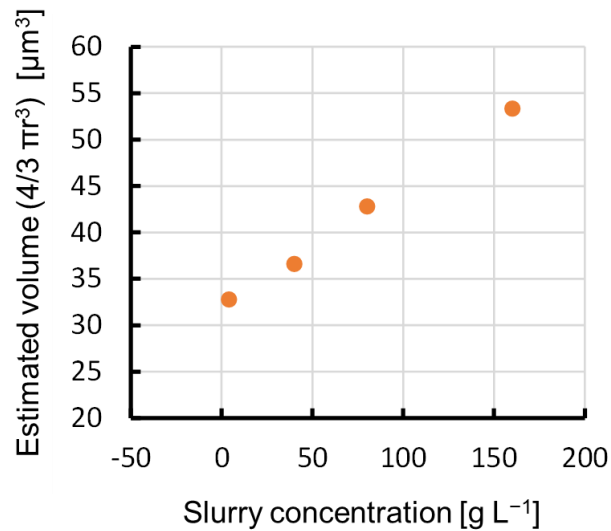[1]Calculated from the weight of a polymer sample in a volumetric cup without tapping.

**Figure 1.  Feeding slurry concentration vs. estimated volume of secondary agglomerated particles.**

It was found that the particle size of the resulting secondary agglomerated particles could be controlled by adjusting the feeding slurry concentration. Therefore, four secondary particles (S-MgO-X, where X is the feeding slurry concentration: 4, 40, 80, or 160 g L-1) were catalyzed by treating them with $TiCl_4$ (S-Cat-X). SEM images of S-MgO and S-Cat are shown in Figure 2. All the S-MgO samples obtained by spray drying were spherical, and there was no change in the morphology of the particles after catalyzing with $TiCl_4$. The particle size distribution is shown in Figure 3. The control sample, MgO50 (raw material), showed agglomeration in heptane to show a broad peak at about 10 μm. On the other hand, S-MgO sample formed by spray drying did not aggregate in heptane and was monodisperse, as was the sample with the MgO surface modified with surfactant (PA-MgO50). This can be attributed to the fact that the dispersive force exceeds the electrostatic cohesive force due to the significant reduction in the apparent surface area relative to the apparent volume of the secondary particles. After catalyzing the support, the S-Cat samples showed almost the same particle size and distribution as the S-MgO samples, confirming that the catalytic process did not cause any morphological deterioration such as particle fragmentation.
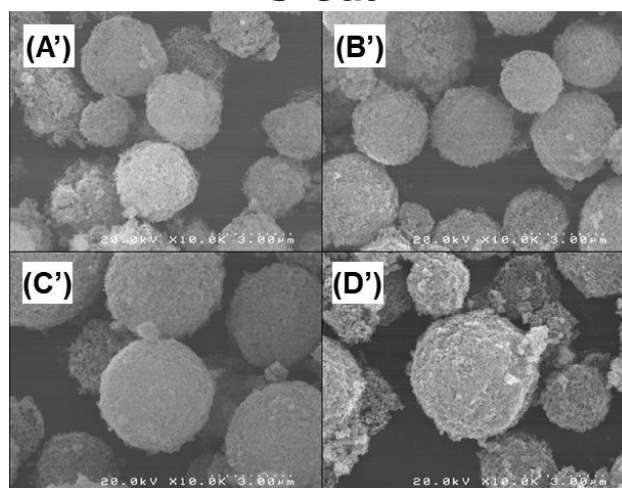
## S-MgO
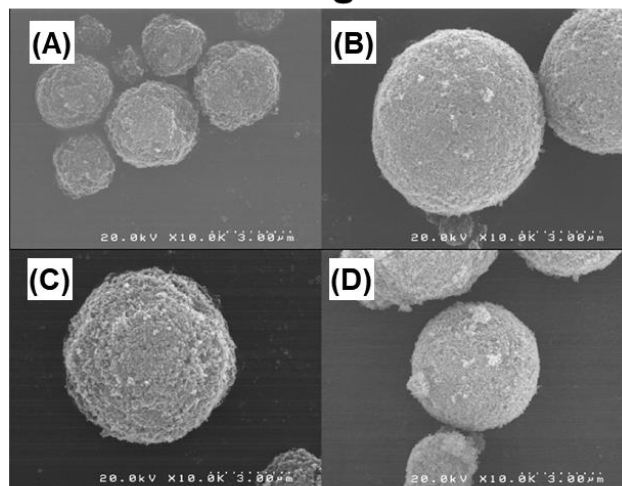


## S-Cat



**Figure 2.** **SEM image of A) S-MgO-4, B) S-MgO-40, C) S-MgO-80, D) S-MgO-160, A') S-Cat-4, B') S-Cat-40, C') S-Cat-80 and D') S-Cat-160.**
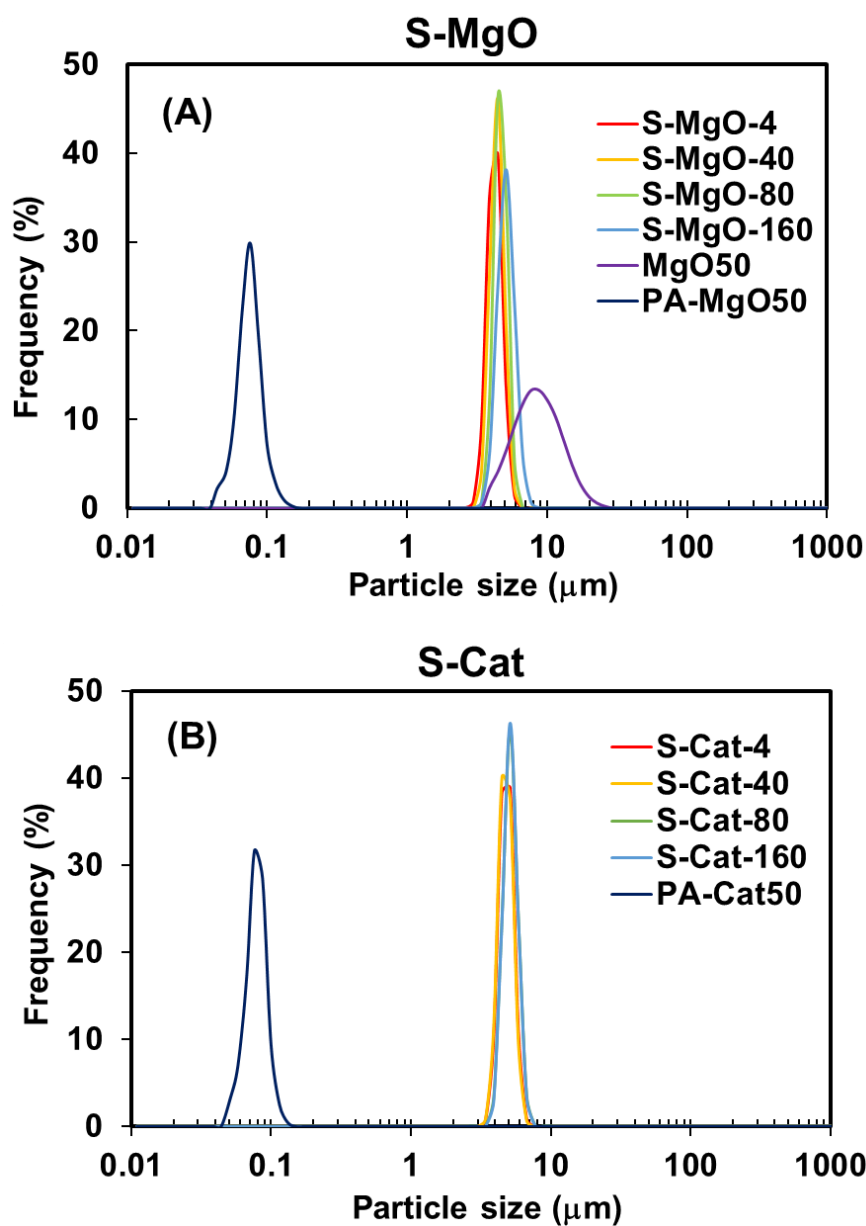
**Figure 3.** Particle size distribution of A) S-MgO samples and MgO modified with surfactant and B) S-Cat samples and MgO based catalyst modified with surfactant.

The results of nitrogen adsorption analysis of the S-Cat samples are shown in Figure 4.

All the samples show type IV adsorption isotherms, and there is almost no hysteresis,

indicating that S-Cat samples are free from micropores or mesopores. Next, the results of

mercury porosimetry are shown in Figure 5. The mercury porosimetry is a method to

obtain information on the size and distribution of pores in the sample on the basis of the

high surface tension and contact angle of mercury (the larger the pore, the lower the

pressure at which the mercury penetrates). Figure 5A shows the cumulative distribution

of the amount of mercury injected against the applied pressure. All the samples showed a

similar behavior, that is, there were two intense mercury injection at between 100 and 200

psi and at between 1000 and 3000 psi.

Figure 5B shows the pore size distribution assuming that the pores in the sample are

either cylindrical or slit-shaped [9] (Equations 6 and 7),

$$R = 2\sigma cos\theta / P \qquad (6),$$

$$W = 2\sigma cos\theta / P \qquad (7),$$

where $R$ is the pore radius, $W$ is the width of the slit, $\sigma$ is the surface tension of mercury

(0.485 Pa m), $\theta$ is the contact angle of mercury (130°), and $P$ is the applied pressure.

Since the right-hand side is the same for both cylindrical and slit shapes, the result will

be the same in either case. Two major peaks are appeared in the pore size distribution,

reflecting the two intense injections seen in Figure 5A. The peak over 0.06 to 0.11 μm is

termed as Peak 1, and the peak over 0.8 to 1.3 μm is termed as Peak 2. Since the diameter

of the MgO primary particles is ca. 0.05 μm (50 nm), Peak 1 is thought to originate from

the pores between the aggregated primary particles. On the other hand, considering that

the diameter of the secondary particles is 4-5 μm, the latter is unlikely to be pores inside

the particles. The SEM image of the cross-section of the particles shown in Figure 6 is

also consistent with this consideration.

If the sample is spherical and has a uniform particle size, the particle size can be

estimated from the pressure at which mercury permeates the interstices among the

particles [10] (Equation 8).

$$P = fKr/d \quad (8),$$

where, $P$ is the applied pressure, $r$ is the surface tension of mercury (0.485 Pa m), and $f$

is the shape factor of the particles, which is 1 if the particles are spherical, and 1 here

because the secondary agglomerates are spherical as shown in Figure 2. $K$ is a constant

that depends on the packing ratio of the particles. Here, 10.73 is applied as commonly

used value for spherical particles. The particle size distribution obtained using Equation

8 is shown in Figure 5C. Similarly, two peaks appeared, reflecting the two intense

injections seen in Figure 5A: the peak at 0.1-0.7 μm is designated as Peak 1, and the peak

at 2-7 μm is designated as Peak 2. Peak 2 corresponds well with the particle size

determined by light scattering method and SEM (Table 1 and Figure 2). Peak 1 is

significantly different from the diameter of the primary particles (0.05 μm), but this is

probably because the shape of the primary particles is cubic and Equation 8, which

assumes spherical particle packing, cannot be applied. The values determined from each

peak top are summarized in Table 2. From the above discussion, it can be concluded that

the two intense injections of mercury seen in Figure 5A is due to the gap among the

secondary particles and the gap between primary particles from the low pressure side,

respectively. The amount of mercury injection at each stage is summarized in Table 3.

From S-MgO-4 to S-MgO-160, the pore diameter inside the secondary agglomerated

particles (Table 2, pore diameter-Peak 1) decreased from 0.11 to 0.06 μm, indicating that

the higher the feed slurry concentration, the denser the particles tend to be. On the other

hand, the injection amount of mercury corresponding to Peak 1 tended to increase with

the feed slurry concentration (Table 3), which corresponds to the increase in secondary

particle diameter (Table 1, Figure 1). The particle diameter calculated from Peak 2 (Table

2, particle diameter-Peak 2) became smaller as the slurry concentration increased. This is

the opposite trend of the particle diameter determined by light scattering. Since the

amount and pressure of mercury injected depends on the packing of the particles, it is

expected that the thinner the slurry concentration, the looser the packing of the secondary

particles. The slightly smaller particle size and slightly larger pore size inside the particles

(lower density) may make them more susceptible to static electricity, and the loose

packing between primary particles may also affect the roughness of the secondary particle

surface, which causes loose packing. In any case, two points seem to be related to the

increase in bulk density: less voids inside the secondary particles and better packing
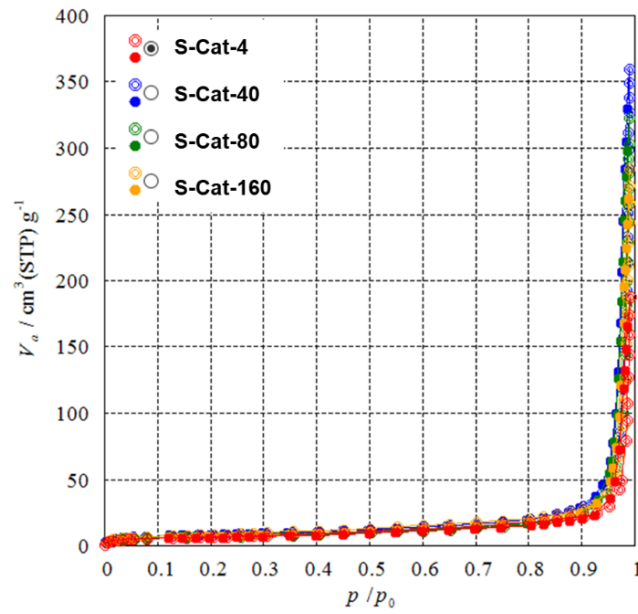
between the secondary particles.



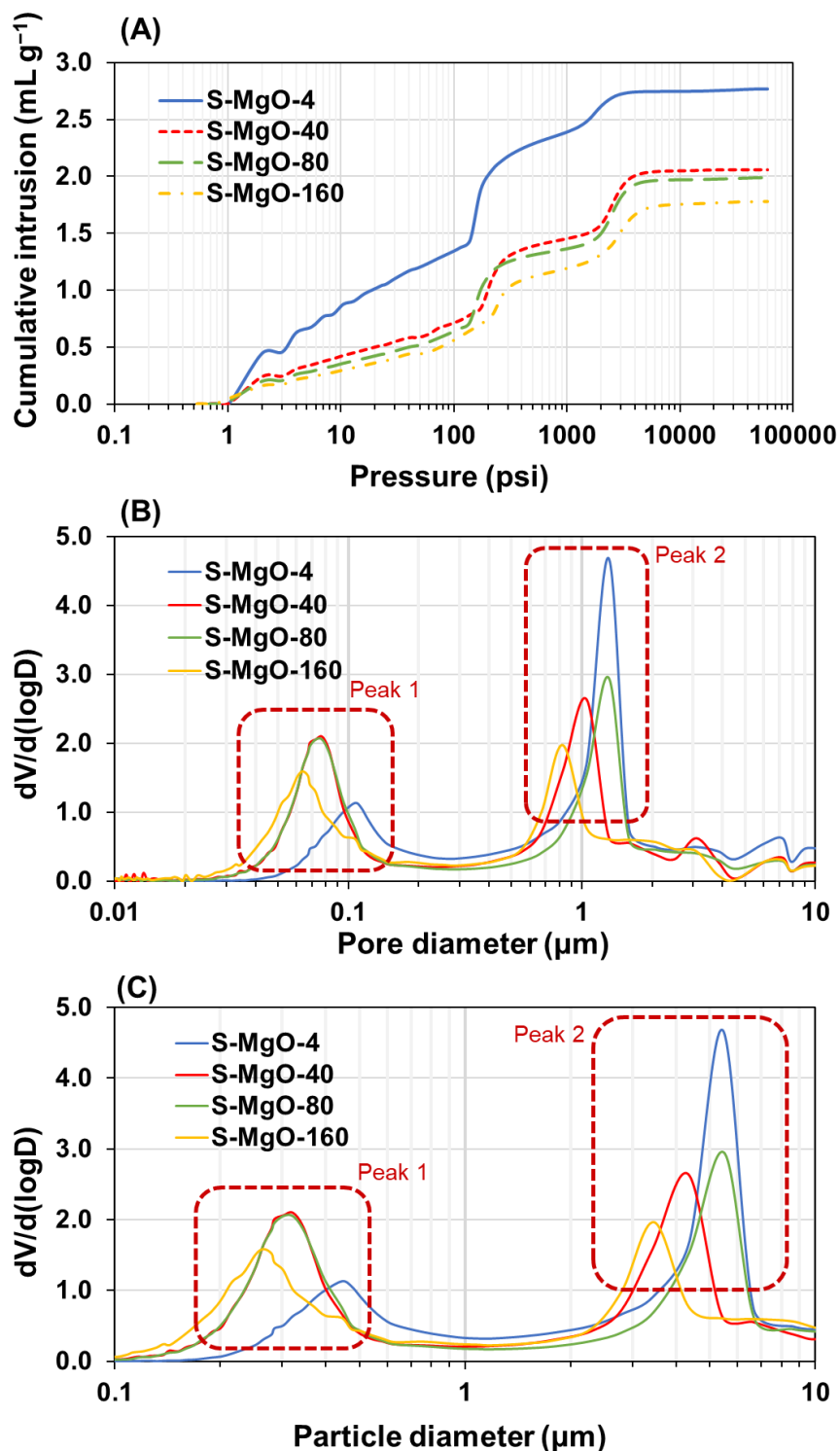**Figure 4.** **N$_2$ adsorption/desorption isotherm of S-Cat samples**

**Figure 5.** **Results of mercury porosimetry of S-MgO samples. A) Cumulative intrusion of mercury at applied pressure, B) calculated pore diameter assumed cylindrical or slits, and C) calculated particle diameter.**

**Table 2. Pore diameter and particle diameter estimated from the mercury intrusion.**

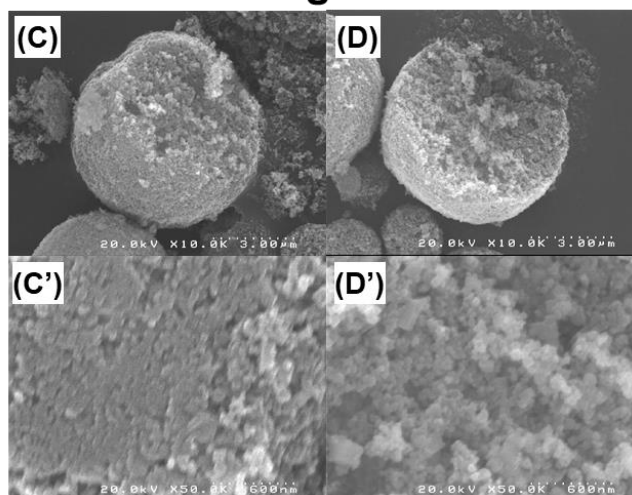| Sample | Pore diameter | | Particle diameter | |
|---|---|---|---|---|
| | Peak 1 ($\mu$m) | Peak 2 ($\mu$m) | Peak 1 ($\mu$m) | Peak 2 ($\mu$m) |
| S-MgO-4 | 0.11 | 1.30 | 0.44 | 5.43 |
| S-MgO-40 | 0.08 | 1.04 | 0.32 | 4.34 |
| S-MgO-80 | 0.07 | 1.31 | 0.30 | 5.48 |
| S-MgO-160 | 0.06 | 0.83 | 0.27 | 3.46 |
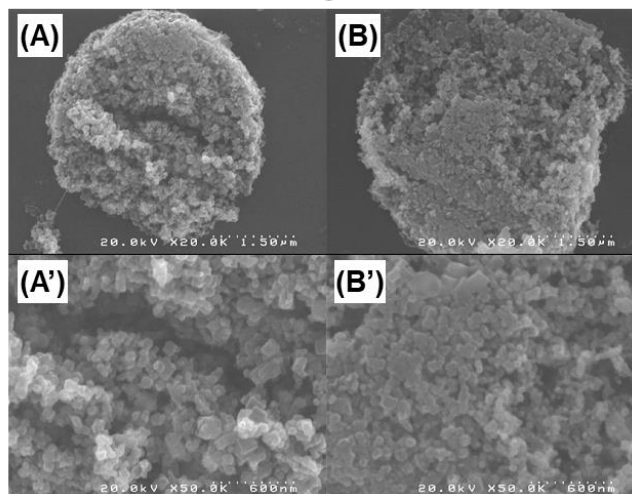


**Figure 6.    SEM image of cross section of the spray dried particles. A,B,A',B') S-MgO-4, C,D,C',D') S-MgO-40.**

79

**Table 3. Mercury porosimetry analysis result for S-MgO samples**

| Sample | Bulk density | | Mercury intrusion volume | | |
| --- | --- | --- | --- | --- | --- |
| | Apparent[1] (g mL$^{-1}$) | Mercury porosimetry (g mL$^{-1}$) | Total intrusion (mL g$^{-1}$) | Pore volume (mL g$^{-1}$) | Interparticle space (mL g$^{-1}$) |
| S-MgO-4 | 0.166 | 0.309 | 2.76 | 0.514 | 0.878 |
| S-MgO-40 | 0.180 | 0.405 | 2.06 | 0.694 | 0.625 |
| S-MgO-80 | 0.206 | 0.429 | 1.99 | 0.696 | 0.630 |
| S-MgO-160 | 0.213 | 0.448 | 1.78 | 0.687 | 0.505 |

[1]Calculated from the weight of a polymer sample in a volumetric cup without tapping during filling a polymer sample.

UHMWPE was synthesized using the S-Cat samples (Table 3). The Ti content of both S-Cat samples was about 0.3 wt%, which is lower than that of PA-Cat50, a core-shell MgO/MgCl$_2$/TiCl$_4$ catalyst with surface modification in a previous study, due to the absence of organic modification (complexation of surfactant with TiCl$_4$). The polymerization activity of the S-Cat samples was about 2500-2700 g-PE g-Cat$^{-1}$. The reason for the constant activity among the catalysts can be attributed to the fact that the properties of each catalyst primary particles were almost the same and there were no micropores involved in the diffusion rate-limiting of monomers and co-catalysts. The polymer particles obtained were spherical in shape, just like the catalyst used. The surface of the particles was covered with a fibril-like polymer, which was probably obtained by extrusion of the polymer grown inside the particles through the pores [11]. Table 5 shows

the results of the characterization of the synthesized polymers. The bulk density of the

polymers showed a trend corresponding to the bulk density of the S-MgO samples used.

There was almost no difference in the molecular weight of each polymer sample, which

was about $4.0 \times 10^6$ g mol$^{-1}$. DSC analysis (Figure 6) showed that the melting temperature

($T_m$, nascent) of the nascent polymer was 141-143 °C, and the melting temperature ($T_m$,

melt-crystallized) of the polymer after the second heating was 134-136 °C. The results of

molecular weight and melting temperature were almost the same as those of UHMWPE

synthesized by PA-Cat50, suggesting that similar PE can be synthesized by S-Cat.
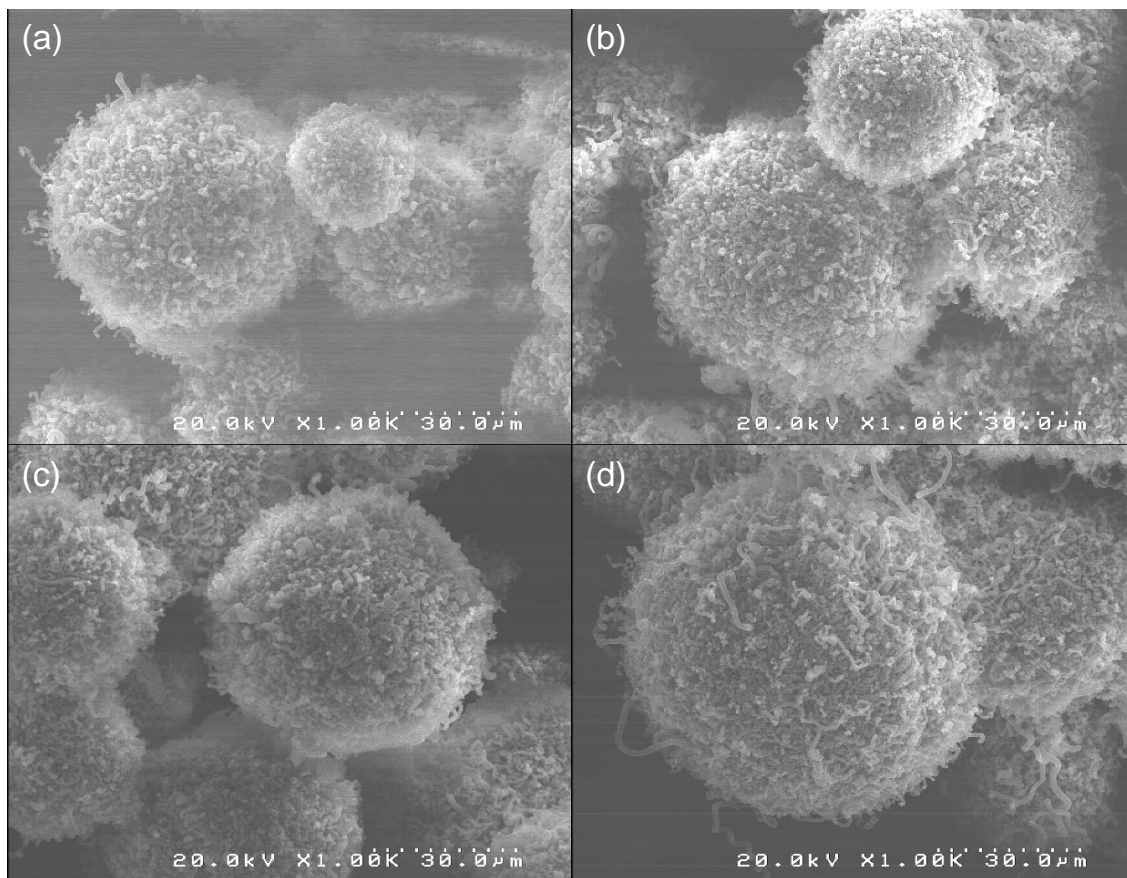
**Figure 6.** SEM image of a) S-PE-4, b) S-PE-40, c) S-PE-80 and d) S-PE-160.

**Table 4. Catalyst particle characterization and ethylene polymerization performance.**

| Sample | Particle size | | | RSF | Ti content (wt%) | Activity (g-PE g-Cat$^{-1}$) |
|---|---|---|---|---|---|---|
| | $D_{10}$ (mm) | $D_{50}$ (mm) | $D_{90}$ (mm) | | | |
| S-Cat-4 | 3.85 | 4.48 | 5.24 | 0.31 | 0.34 | 2780 ±80 |
| S-Cat-40 | 3.80 | 4.44 | 5.14 | 0.30 | 0.33 | 2230 ±220 |
| S-Cat-80 | 4.06 | 4.79 | 5.66 | 0.33 | 0.29 | 2750 ±30 |
| S-Cat-160 | 4.07 | 4.79 | 5.65 | 0.37 | 0.32 | 2670 ±190 |
| PA-Cat50 | 0.058 | 0.073 | 0.090 | 0.44 | 0.76 | 3200 |

**Table 5. Properties of polymer samples**

| Sample | Polymer bulk density[1] (g cm$^{-3}$) | $M_v$ ($\times 10^6$ g mol$^{-1}$) | $T_m$, nascent (°C) | $T_m$, melt-crystallized (°C) |
|---|---|---|---|---|
| S-PE-4 | 0.088 | 3.9 | 140.7 | 133.9 |
| S-PE-40 | 0.101 | 4.0 | 140.6 | 133.7 |
| S-PE-80 | 0.118 | 3.9 | 140.8 | 133.8 |
| S-PE-160 | 0.121 | 4.2 | 141.5 | 134.2 |
| PA-PE50 | 0.121 | 3.7 | 142.6 | 135.5 |

[1]Calculated from the weight of a polymer sample in a volumetric cup without tapping during filling a polymer sample.
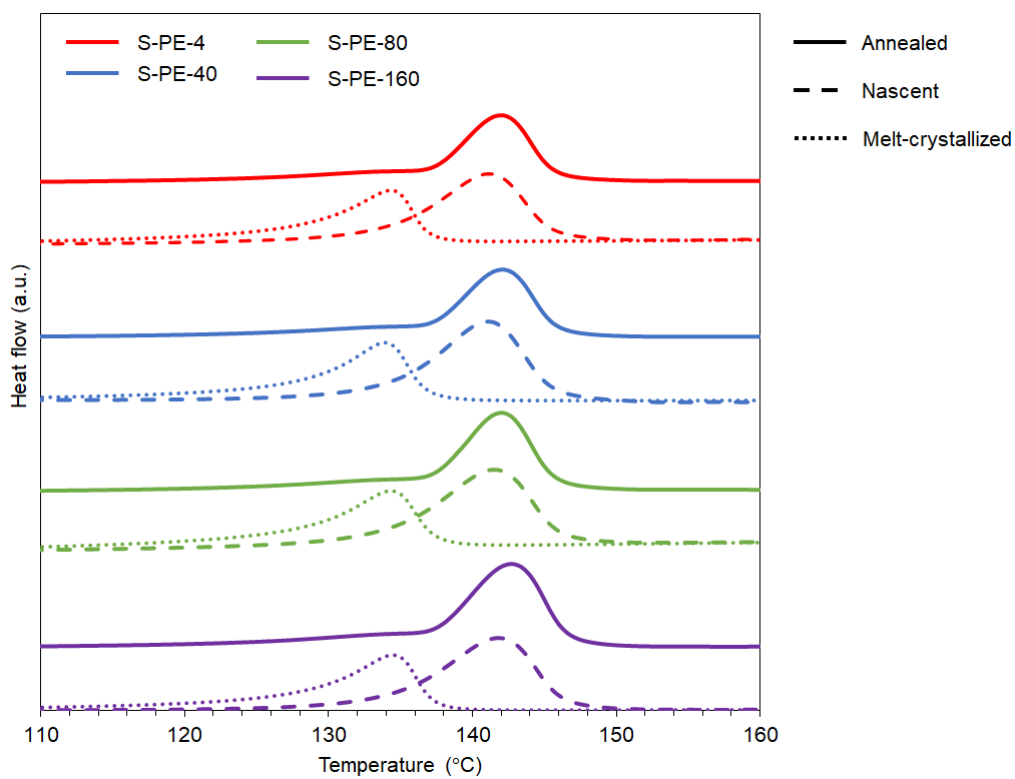


**Figure 7.    DSC analysis for PE samples produced by S-Cat samples.**

In order to investigate the processability of the polymer particles synthesized from the S-Cat samples, each polymer sample (S-PE-X, where X is the feeding slurry concentration condition of the catalyst used) was compressed into a film at 120 °C. As shown in Figure 8, all polymer samples obtained with S-Cat started to melt at 120 °C and translucent regions were observed. This fusion initiation temperature is the same as the lowest fusion initiation temperature to that of the polymer obtained from PA-Cat50 [3].

In summary, S-Cat enables the synthesis of UHMWPE with excellent molding processability like PA-Cat50, and polymer particles with small electrostatic effect can be obtained due to the larger polymer particle size. In addition, unlike PA-Cat50, S-Cat can be dispersed in hydrocarbon solvents without the need for organic modification, thus avoiding the use of surfactants, which are catalyst poisons. Thus, microfine grade of UHMWPE particles were obtained by catalyst synthesized through spray dried MgO nanoparticle.
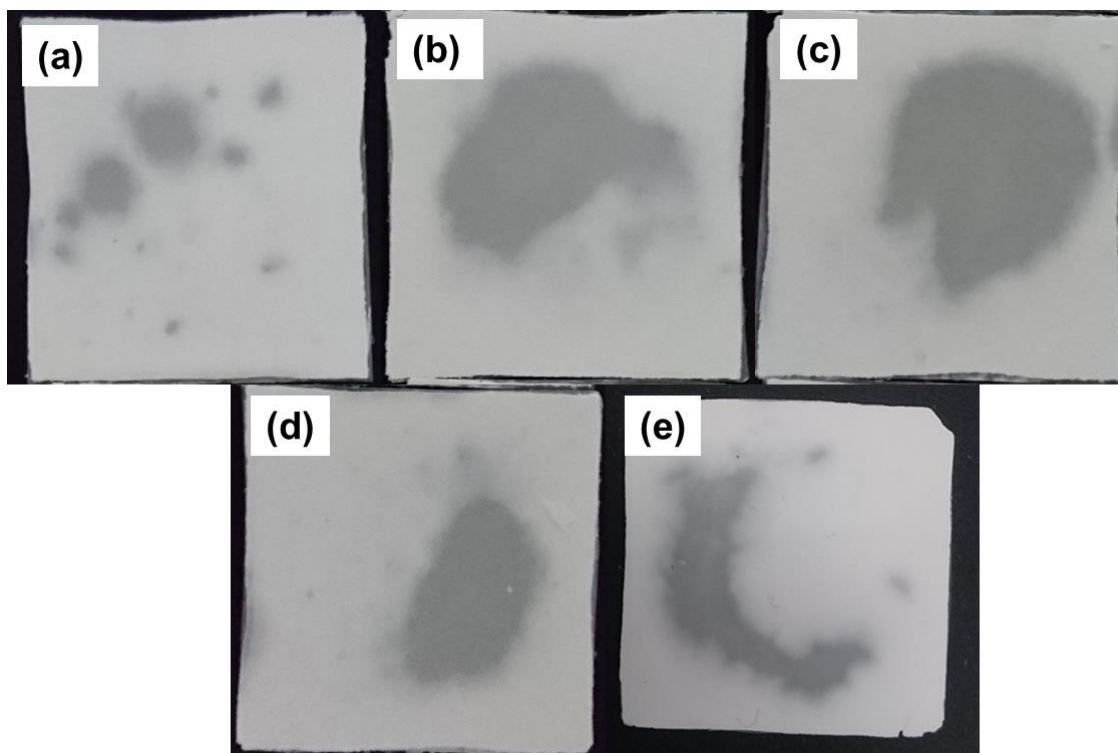
**Figure 7. Compression-molded polymer reactor powder at 120 °C. a) S-PE-4, b) S-PE40, c) S-PE-80, d) S-PE-160, and e) PA-Cat50.**

## *3.4. Conclusions*

Secondary agglomerated particles (S-MgO) were prepared using a spray dryer from MgO nanoparticles. When the concentration of MgO slurry fed to the spray dryer was increased from 4 g $L^{-1}$ to 160 g $L^{-1}$, the diameter of the secondary particles increased from 3.7 μm to 4.7 μm and the bulk density increased from 0.17 g $cm^{-1}$ to 0.21 g $cm^{-1}$. All the obtained S-MgO samples were spherical in shape and the particle size distribution was quite narrow. From the nitrogen adsorption test, it was found that the S-MgO samples had only macropores. By increasing the feed slurry concentration, the pore size inside the

85

secondary particles decreased from about 0.1 μm to about 0.06 μm. The breakthrough

pressure of mercury involved in the voids between the secondary particles decreased as

the feed slurry concentration increased, indicating that the higher the feed slurry

concentration, the better the packing of the secondary particles. The prepared S-MgO

samples was converted to catalysts (S-Cat) for ethylene polymerization. There was almost

no difference in activity among the catalyst samples. The obtained PE particles were

spherical in shape, mimicking the shape of the catalyst, and had a molecular weight of

about $4.0 \times 10^6$ g mol$^{-1}$. When a film was prepared by compression molding using each

polymer sample, it was observed that the films started to melt at 120 °C, similar to the PE

synthesized by PS-Cat50 in the previous study. In this study, the bottom-up preparation

method using a spray dryer resulted in a spherical catalyst with a smaller particle size and

narrower size distribution than the conventional Ziegler-Natta catalyst, thus ultra-fine

grade of UHMWPE particles has been available. The bottom-up preparation method is

more advantageous in controlling the morphology of the catalyst, and its future

development will make it possible to simplify the preparation of particulate catalysts that

require complex processes.

## Reference

[1] L. A. Pruitt, Oxford: Elsevier, 2017, 1.23-Load-Bearing Medical Polymers (Non-degradable). In Comprehensive Biometerials II, p 507-515.

[2] E. Albizzati, U. Giannini, G. Collina, L. Noristi, L. Resconi, Cincinnati (Ohio, USA): Hanser-Gardner Publications, 1996, Catalysts and polymerizations. In Polypropylene Handbook, Moore, E. P. J., Ed.

[3] P. Chammingkwan, Y. Bando, M. Terano, T. Taniike, *Front. Chem.* **2018**, 6, 524.

[4] US 4972035, Mitsui Petrochemical Industries, 1990.

[5] US2010/0196711, Ingersoll & Rooney PC, 2010.

[6] US 7601423, Mitsui Petrochemical Industries, 2009.

[7] T. Ikeda, T. Wada, Y, Bando, P. Chammingkwan, T. Taniike, *Catalysts*, **2021**, 11, 1092 (pp. 1-13)

[8] L. Bayvel, Z. Orzechowski, Boca Raton: Routledge, 2019, Liquid Atomization.

[9] M. Takahashi, L. Weiren, *Shigen-to-Sozai*, **2004**, 120, 455-460.

[10] M. Asaki, M. Morimoto, C. A. Leon y Leon, *J. Soc. Powder Technol., Japan,* **1998**, 35, 566-572.

[11] K. Kageyama, J. Tamazawa, T. Aida, *Science*, **1999**, 285, 5436, 2113-2115.

# *Fabrication of Multi-Grained MgO/MgCl$_2$/TiCl$_4$/donor Core–Shell Catalyst for Stereospecific Propylene Polymerization*

## 4.1. Introduction

Ziegler-Natta catalysts (ZNC) for the industrial production of isotactic polypropylene (PP) have a complex structure consisting of $TiCl_4$ and organic donors (e.g., esters and ethers) co-adsorbed on a highly disordered $MgCl_2$ support. Activation usually requires the reaction of trialkyl alminium (e.g., $AlEt_3$) complexed with a second donor (e.g., alkoxysilane). Since the discovery the above combination, the catalytic system has been improved, giving various generations of catalysts with different electron donors to improve their performance [1].

In the early 1960s, ZNCs were less active and had low stereospecificity (I.I. < 50%), making the commercial production of PP difficult; in the late 1960s, catalysts co-milled with $MgCl_2$, $TiCl_4$, and organic Lewis bases called internal donors were developed. The use of trialkylaluminum in combination with a Lewis base, called an external donor, during polymerization resulted in higher activity and high stereospecificity [2]. In the 1980s, new combinations of electron-donating compounds were developed. Catalysts using alkyl phthalates as internal donors and alkoxysilanes or silyl ethers as external donors showed further improvements in activity and stereoregularity [3]. In the late 1980s, catalysts using 1,3-diether compounds as internal donors was developed. In the late 1980s, catalysts using 1,3-diether compounds as internal donors were developed, which showed

high activity and stereospecificity without the need for external donors [4]. In the late 1990s, a catalyst using succinate as an internal donor was developed, and by using alkoxysilane as an external donor, PP with a wide molecular weight distribution can be synthesized [5,6].

The control of polymer morphology is also very important in the production of PP. When the polymer particles have ideal morphology, such as high density, regular shape, and narrow particle size distribution (PSD), they exhibit favorable properties in the production process, such as high productivity, good flowability and packability. It is well known that the size, shape and PSD of polymer particles can be controlled to some extent by the catalyst used. Usually, the polymer tends to magnify and replicate the shape and structure of the catalyst used, which is called the replica effect [7-9].

In our previous work, we have also prepared supports with multigrain structure by granulating MgO particle nanoparticles into secondary particles using a spray dryer. By using this technique, it is possible to prepare catalysts with spherical shape and narrow PSD. However, since MgO-derived catalysts do not contain donors, their stereoselectivity is low, and previous studies have reported the synthesis of PP with low stereoregularity [10]. In this chapter, propylene polymerization with internal and external donors was carried out with the aim of synthesizing PP with high stereoregularity using MgO-derived

catalysts prepared by spray-drying method.

## *4.2. Experimental*

### *4.2.1. Materials*

MgO with the mean particle size of 50 nm (Wako Pure Chemical Industries Ltd.) were used after dehydration at 160 °C under $N_2$ flow.  Titanium tetrachloride ($TiCl_4$) of research grade was used as received.  Di-*n*-butylphthalate (DBP) and *n*-Heptane were used after dehydration by $N_2$ bubbling over 4A molecular sieve. Propylene of polymerization grade (Japan Polypropylene Co., Tokyo, Japan) was used as received. Cyclohexylmethyldimethoxysilane (CMDMS) was purified by distillation under reduced pressure. Triethylaluminium (TEA, donated by Tosoh Finechem Co.) was used after dilution in heptane.

### *4.2.2. Preparation of Catalyst Support*

Pristine MgO nanoparticles were dispersed in methanol by means of ultrasonication for 6 h to prepare a feeding slurry of 4 g $L^{-1}$. The feeding slurry was introduced into the atomizer by a peristaltic pump and sprayed into the main chamber by compressed air. The sprayed droplets were dried by hot air in the main chamber where extremely large dried

particles fell into the separation container, and the rest were carried over to the cyclone.

Particles of a certain size were collected as a spray-dried product (denoted as S-MgO) by

centrifugal force, and fine particles were flown out to the exhaust line. The spray drying

conditions were: inlet temperature = 160 °C, feed rate = 800 mL h$^{-1}$, atomization air

pressure = 20 ×10 kPa, and blower rate = 0.3m$^2$ min$^{-1}$.


## 4.2.3. Catalyst Preparation

0.5 g of S-MgO was heated at 130 °C under N$_2$ flow for 6 h to remove physisorbed

water before treating with 30 mL of TiCl$_4$ at the reflux temperature for 2 h. The obtained

product (denoted as S-Cat A, donor free catalyst) was washed with heptane repetitively

and stored as a slurry under N$_2$. Besides C-Cat A, more two catalyst samples (C-Cat B

and C-Cat C) were prepared as donor containing catalysts (Scheme 1). After TiCl$_4$

treatment, 20 ml of TiCl$_4$ was removed, and then 0.16 mmol of DBP and 20 ml of toluene

were introduced and heated at 90 °C for 2 hours. The resulting product was washed with

toluene and heptane to prepare C-Cat B. In the preparation of C-Cat C, the carrier was

treated with TiCl$_4$ as in C-Cat B, followed by treatment with DBP and toluene. After

washing the obtained product with toluene, 10 mL of toluene and 10 mL of TiCl$_4$ were

added and heated at 90 °C for 2 hours. And finally, the remaining product was washed

with toluene and heptane to prepare C-Cat C.
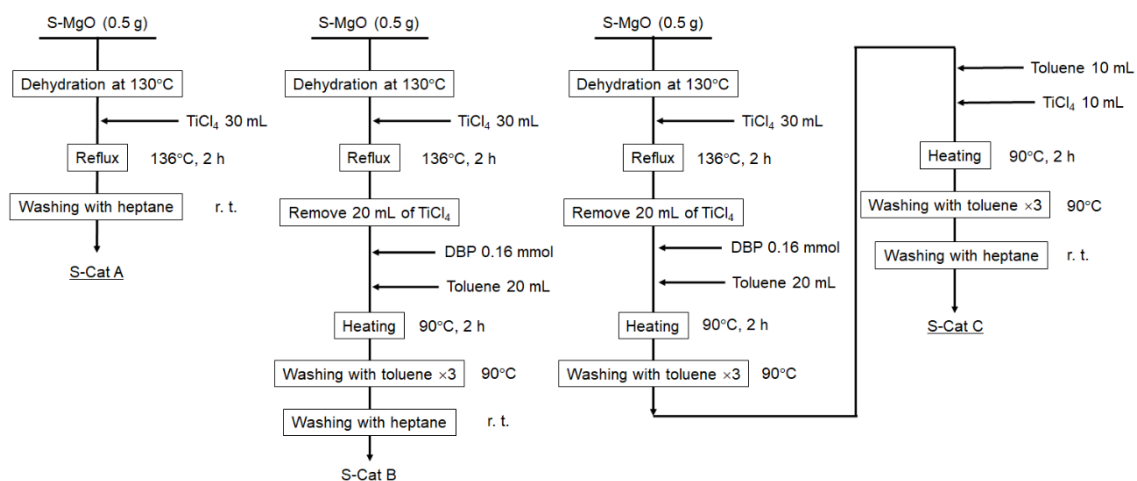


**Scheme 1  Preparation of S-Cat A, S-Cat B and C-Cat C.**

## 4.2.4. Polymerization

Propylene polymerization was performed in a 1 L stainless steel autoclave equipped with a mechanical stirrer rotating at 500 rpm. After sufficient $N_2$ replacement, 300 mL of heptane as a solvent was introduced to the reactor and then saturated with 0.5 MPa of propylene at 50 °C for 30 min. Following the addition of 2.0 mmol of TEA as a co-catalyst and CMDMS as an external donor, ca. 70 mg of a catalyst was introduced to initiate polymerization. The polymerization was performed at 50 °C for 30 min at the constant pressure of 0.5 MPa. After 30 min of polymerization, the obatined polymer was filtered and dried in vacuum oven at 60 °C for 6 h. The remaining solvent was introduced into

cold acetone and the reprecipitated polymer was collected and dried.

## 4.2.5. Characterization

The morphology of the supoourt samples, the catalyst samples, and polymer particles was observed by scanning electron microscopy (SEM, Hitachi S-4100) performed at an accelerating voltage of 20 kV. Before the measurements, particles were subjected to Pt sputtering for 90 s. The particle size distribution profiles of support and catalyst samples were acquired from a light scattering (Horiba Partica LA-950V2). The measurements were done in a suspension from using $n$-heptane as a medium. The particle size was expressed as D10, D50, and D90, which corresponded to the particle size at 10, 50, and 90% of the cumulative volume distribution. A relative span factor (RSF) was calculated based on Equation (1):

$$\text{RSF} = \frac{D_{90} - D_{10}}{D_{50}} \qquad (1)$$

The Ti content was determined by UV–vis spectroscopy (V-770, JASCO, Tokyo, Japan). A measured amount of a catalyst was dissolved in $HCl/H_2SO_4$ solution, and then $H_2O_2$ was added to form a Ti–peroxo complex that exhibits the absorbance of the ligand metal charge transfer at 410 nm. The Ti content was analyzed from the intensity of the

spectrum peak located at 410 nm using a pre-determined standard curve.

The catalyst samples and the polypropylene samples were analyzed by NMR (Bruker 400 MHz) operated at 25 °C and 120 °C, respectively. For the catalyst sample analysis, about 10 mg of the sample was dissolved in 0.5 mL of DMSO-d$_6$ and 0.2 mL of 1,1,2,2-tetrachroloethane. The peak integral of 1,1,2,2-tetrachloroethane at 7.00 ppm in $^1$H NMR was used as an internal standard for quantifying the organic components of a catalyst. For the PP sample analysis, about 40 mg of the sample was dissolved in 0.2 mL of 1,1,2,2-tetrachloroethane-$d$2 and 0.5 mL of 1,2,4-trichlorobenzene containing 0.006 wt.% of 2,6-di-tert-butyl-4-methylphenol (stabilizer for heat degradation of polymer). The stereoregularity of PP unit (*mmmm*) in the polymers was determined by the methyl peaks in the $^{13}$C NMR spectrum.

## 4.3. Results and Discussion

To confirm the donor content of the catalyst samples, $^1$H NMR measurement was carried out (Figure 1). The peaks attributed to DBP and the byproduct butoxide were observed. The donor content of S-Cat B and S-Cat C was about 2 wt% and 1 wt%. The Ti/DBP ratio of S-Cat B and S-Cat C was about 1 and 2. By the additional TiCl$_4$ treatment, the donor content was reduced.
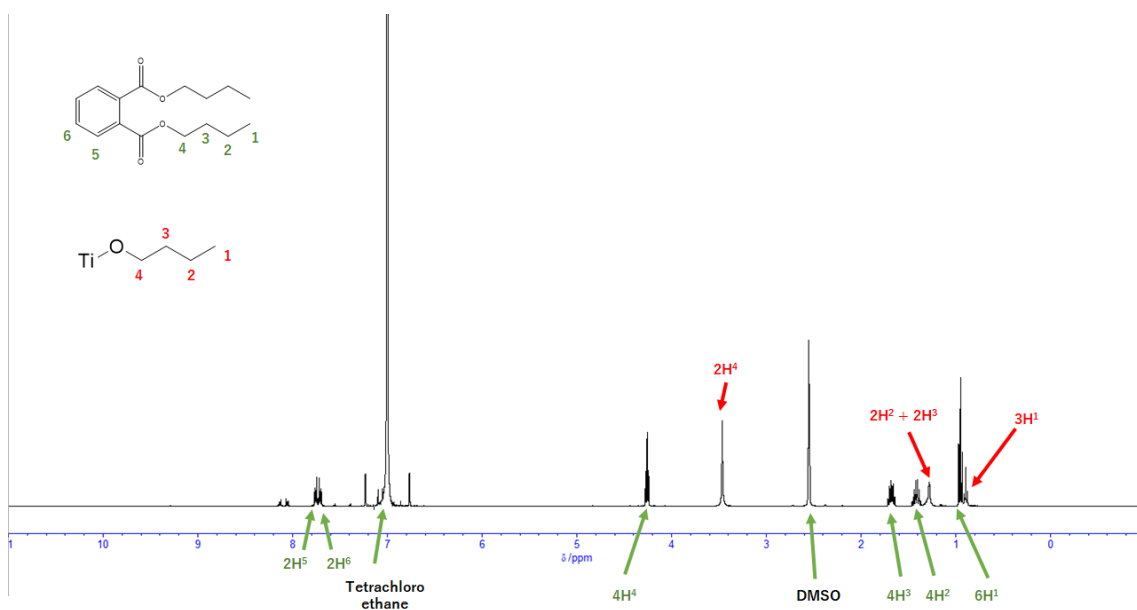


**Figure 1. $^1$H NMR spectrum of S-Cat B**

The PSD and the morphology of S-Cat B and S-Cat C was analyzed by a laser diffraction particle size analyzer and SEM. The particle size distribution of S-Cat B and S-Cat C was similar with the original S-Cat A. In SEM image (Figure 3), MgO nanoparticles can be seen on the surface of S-Cat B and S-Cat C. S-Cat B and S-Cat C were successfully prepared without fusion of MgO particles.

The property of catalyst and the result of polymerization were listed in Table 1 and Table 2. The activity was decreased with the content of DBP in the absence of external donor. On the contrary the soluble part of polymer collected by a reprecipitation decreased with the content of DBP. There was little difference in the mesopentad fraction of each soluble and insoluble part of PP obtained by each catalyst sample. By the reduction of soluble part of polymer, the total mesopentad fraction of PP obtained by the catalyst samples containing DBP improved. When the external donor was used, all catalyst activity was lower than when it was not used. However, the decrease in activity of S-CatA without the internal donor was large, whereas the decrease in activity of S-CatB and S-CatC with the internal donor was small. Moreover, soluble part polymer was not obtained with S-CatB and S-CatC. It is thought that the external donor plays a role in maintaining stereoselectivity by compensating for the internal donor that is desorbed during polymerization. It is likely that DBP treatment made some difference in the environment

near the active species. There was also a difference in the mesopentad fraction of the soluble component PP: 88 mol% for PP obtained with S-CatA, while 95 mol% for PP obtained with S-CatB and S-CatC. The external donor also contributed to the improvement of stereoregularity, and the external donor were necessary for the synthesis of isotactic PP with a mesopentad fraction exceeding 90 mol%.
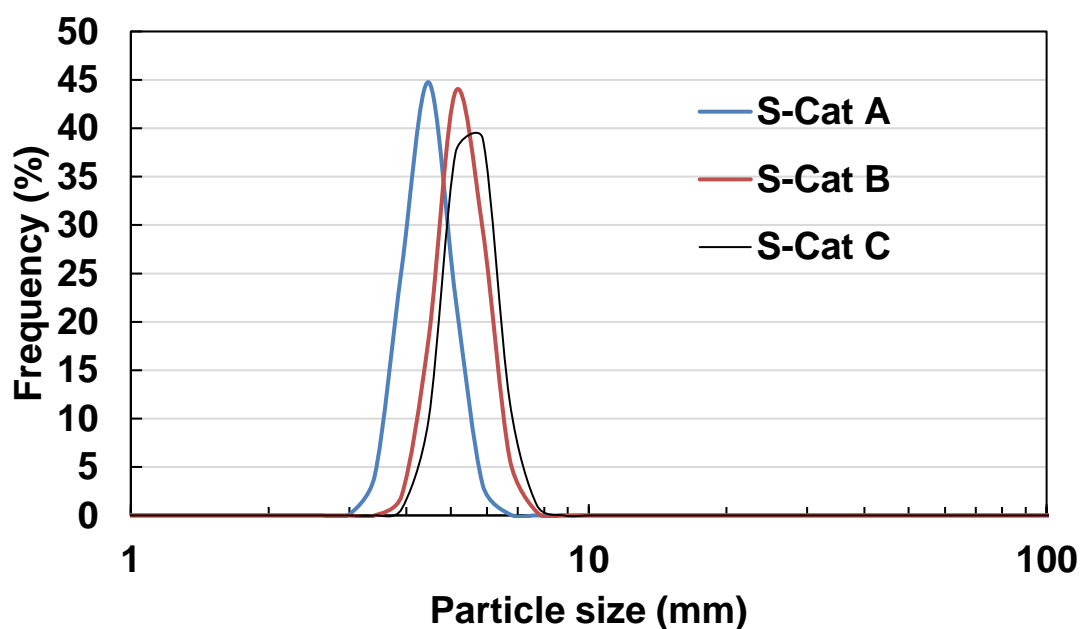


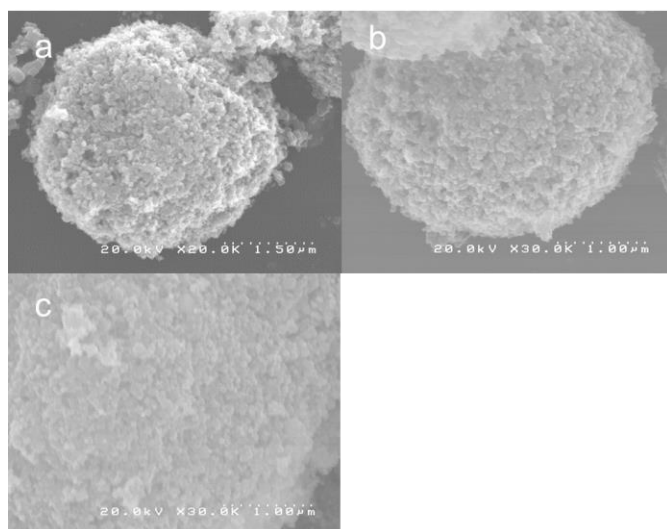**Figure 2. Particle size distribution of catalyst samples**

**Figure 3.   SEM image of a) S-Cat A, b) S-Cat B and c) S-Cat C.**

Table 1.  Property of catalyst samples

| Sample name | Particle size (μm) | Ti content (wt%) | Donor content (mol%) | Ti/DBP (mol/mol) |
|---|---|---|---|---|
| S-Cat A | 4.98 | 0.30 | - | - |
| S-Cat B | 4.90 | 0.56 | 2.85 | 1.14 |
| S-Cat C | 5.16 | 0.35 | 1.06 | 1.93 |

Table 2.   Polymerization results

| Catalyst | E-Donor | Polymer yield (g) | | | Activity (g/mmol-Ti h) | Mesopentad fraction (mol%) | | |
| --- | --- | --- | --- | --- | --- | --- | --- | --- |
| | | Insoluble[1] | Soluble[2] | Total[3] | | Insoluble[1] | Soluble[2] | Total[4] |
| S-Cat-A | × | 3.25 | 1.97 | 5.23 | 2183 | 80 | 27 | 60 |
| S-Cat-B | × | 1.76 | 0.31 | 2.07 | 878 | 91 | 22 | 81 |
| S-Cat-C | × | 2.80 | 1.00 | 3.80 | 1597 | 89 | 23 | 72 |
| S-Cat-A | ○ | 2.26 | 0.43 | 2.69 | 1094 | 88 | 21 | 77 |
| S-Cat-B | ○ | 1.67 | trace | 1.67 | 710 | 95 | - | 95 |
| S-Cat-C | ○ | 2.86 | trace | 2.86 | 1202 | 95 | - | 95 |

[1]Polymer sample collected as reactor powder.

[2]Polymer sample collected by a reprecipitation with acetone.

[3]Total yield of insoluble part and soluble part polymer.

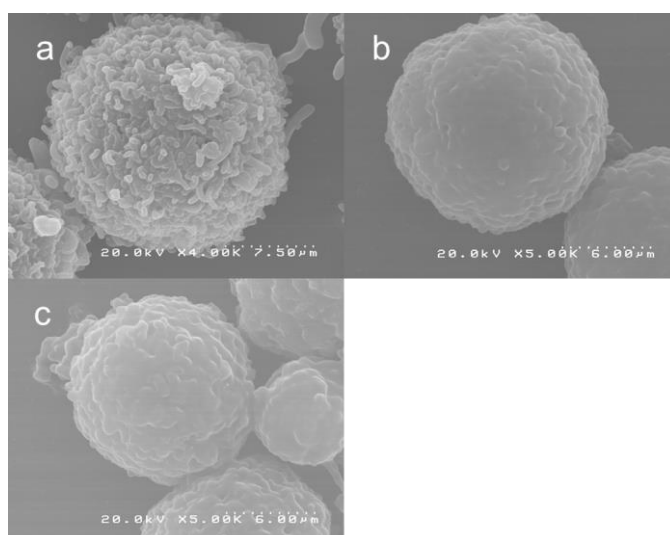[4]Calculuated from the mesopentad fraction of insoluble part and soluble part polymer.



**Figure 2. SEM images of PP particle obtained by a) S-Cat A, b) S-Cat B and c) S-**

**Cat C.**

## *4.4. Conclusions*

In this chapter, donor-doped catalysts were performed to synthesize PP with high stereoregularity even in MgO-derived catalysts. Firstly, MgO nanoparticles were agglomerated by spray drying to prepare secondary MgO macro-particles. The resulting particles were then used to prepare $MgO/MgCl_2/TiCl_4$ core-shell ZNC. DBP was added as an internal donor during the preparation, and the Ti/DBP ratio was varied according to the number of $TiCl_4$ treatments; the DBP content was about 3 % for the catalyst with one $TiCl_4$ treatment (S-Cat B) and about 1 % for the catalyst with two treatments (S-Cat C). The morphology of the primary and secondary particles of the support did not change after the addition of DBP to the catalyst, and the catalyst preparation was achieved while maintaining the morphology of the support. As a result of propylene polymerization without external donor, the activity decreased with the content of DBP. However, the amount of soluble part polymer decreased with the content of DBP, resulting in the improvement of mesopentad fraction. In the presence of the external donor, the activity was decreased compared with the one in the abcence of the external donor. However, the mesopentad fraction improved by the addition of the external donor and PP with the 95 mol% of the mesopentad fraction was obtained by the catalyst samples containing DBP.

## Reference

[1] *Polypropylene Handbook: Polymerization, Characterization, Properties, Processing, Applications*; Moore, J. E. P., Ed.; Hanser Publishers: Munich, Germany, **1996**.

[2] Belgian Patent 785 332, **1972** Montedison.

[3] European Patent 45 977 **1982** Montedison.

[4] U.S. Patent 4 971 937 **1990** HIMONT Incorporated.

[5] Int. Patent WO 00/63261 **2000** Basel Polyolefins.

[6] Cecchin, G., Morini, G., Pelliconi, A., *Macroml. Symp.* **2001**, *173* 195.

[7] Umare, P.; Antony, R.; Gopalakrishnan, K.; Tembe, G. *J. Mol. Catal. A Chem.* **2005**, *242*, 141–150.

[8] Taniike, T., Funako, T., Terano, M., *J. Catal.* **2014**, *311*, 33–40.

[9] Xu, L., Huang, Y.F. Xu, J.Z., Ji, X., Li, Z.M., *RSC Adv.* **2014**, *4*, 1512–1520.

[10] Taniike, T., Chammingkwan, P., Terano, M., *Catal. Commun.* **2012**, *27*, 13-16.

Chapter 5

# *General conclusions*

Ziegler-Natta (ZN) catalysts have a wide range of hierarchical structures, from macro-particles (tens of micrometers) to primary catalyst particles (tens of nanometers) and the surfaces and active sites (sub-nanometers) and it is difficult to separately control the structure at each level. In this study, we established a catalytic system that can realize independent control of only the morphology of macro-particles in ZN catalysts, and explored the application of the obtained catalysts.

Chapter 1 covers the history of heterogeneous Ziegler-Natta catalysts, i.e., the progress and results of scientific investigations into the origin of catalytic function in academia and the improvement of performance in industry.

In Chapter 2, the core concept of this study was demonstrated by bottom-up preparation of spherical catalyst macro-particles by the application of spray-drying on the basis og $MgO/MgCl_2/TiCl_4$ core-shell catalysts whose morphology is inherited from the MgO nanoparticles of the raw material. The spray-dried aggregates of MgO nanoparticles were approximately 5 μm in diameter and spherical in shape, and uniformly dispersed in ethanol without the use of surfactants. The secondary particle catalysts obtained by $TiCl_4$ treatment showed good activity for both ethylene and propylene and produced spherical polymer particles that mimicked the morphology of the catalyst particles. The polymerization kinetics of the secondary particle catalysts was exactly the same as that of the primary particle catalyst, and it was confirmed that the macropores did not contribute to the polymerization kinetics by diffusion limitation.

In Chapter 3, the preparation of microfine grade ultra-high molecular weight polyethylene (UHMWPE) particles was attempted as an application of the secondary particle catalysts. It was found that by increasing the concentration of MgO slurry fed to the spray dryer, the bulk density of the secondary particle catalysts and also of the

obtained UHMWPE particles could be increased. In addition, the obtained UHMPWE particles showed good fusion ability as well as those obtained with the $MgO/MgCl_2/TiCl_4$ core-shell catalyst. As a result, by using this catalyst, I am able to obtain a unique material with microfine grade and low temperature fusion ability.

In Chapter 4, the application of this catalyst to stereospecific propylene polymerization was studied. For the synthesis of α-olefins including propylene, it is important to improve and control the stereoselectivity. By introducing di-*n*-butylphthalate as a donor during the $TiCl_4$ treatment, the stereoregularity of the resulting polypropylene has been improved by about 10 mol% in mesopentad.

In conclusion, I successfully demonstrated that MgO nanoparticles were formed into secondary particles by spray drying and treated with $TiCl_4$ to obtain secondary agglomerated $MgO/MgCl_2/TiCl_4$ core-shell catalyst particles with controlled morphology. The pores originating from the agglomeration of MgO particles with a diameter of 50 nm were found to be so-called macropores with a size of 60 nm-100 nm by mercury intrusion analysis, and it was confirmed that the macropores did not make a significant difference in the catalytic properties and were not related to mass diffusion. In addition, the catalyst was shown to be applicable to the synthesis of microfine grade UHMWPE particles and stereospecific propylene polymerization. On the other hand, the limitation of this study is that only one primary particle could be prepared. The introduction of primary particles of various diameters and morphologies will allow for more precise control of the secondary particle diameter and pores, thus enabling more detailed mechanistic studies. As described above, the multi-grained $MgO/MgCl_2/TiCl_4$ core-shell catalyst established in this study can be used as a basis for future studies on the mechanism of structure-

performance relationship of ZN catalysts and for various applications. We hope that this work will lead to further development of the science of ZN catalysts.

# Achievements

**Publications**

*Original Articles*

1. Tomohiro Ikeda, Toru Wada, Yusuke Bando, Ashutosh Thakur, Patchanee Chammingkwan, and Toshiaki Taniike, Bottom-Up Synthesis of Multi-Grained Ziegler-Natta Catalyst Based on $MgO/MgCl_2/TiCl_4$ Core-Shell Catalyst, *Catalysts*, 11, **2021**, 1092.

**Presentations**

*International Conferences*

1. "Bottom-up synthesis of multi-grain structure of Ziegler-Natta catalyst for kinetic investigation"

5th Blue Sky Conference on Catalytic Olefin Polymerization, Naples and Sorrento, Italy, June, 2019.

*Domestic Conferences*

1. "MgOナノ粒子を用いたZiegler-Natta触媒のマルチグレイン構造の設計"

第49回石油・石油化学討論会（山形大会）、山形、2019年10月

2. "スプレードライ法を利用したMgOナノ粒子由来Ziegler-Natta触媒のボトムアップ合成と超高分子量ポリエチレン合成への利用" 第51回石油・石油化学討論会（函館大会）、北海道、2021年11月

# Acknowledgments